PHYSICAL REVIEW D **112,** 123538 (2025)

Bayesian reconstruction of primordial perturbations from induced gravitational waves

Aya Ghaleb,[1,*] Ameek Malhotra,[1,†] Gianmassimo Tasinato,[1,2,‡] and Ivonne Zavala[1,§]

[1]*Physics Department, Swansea University, SA2 8PP, United Kingdom*
[2]*Dipartimento di Fisica e Astronomia, Università di Bologna, INFN, Sezione di Bologna, viale B. Pichat 6/2, 40127 Bologna, Italy*

(Received 17 June 2025; accepted 5 December 2025; published 24 December 2025)

The formation of primordial black holes or other dark matter relics from amplified density fluctuations in the early Universe may also generate scalar-induced gravitational waves (GW), carrying vital information about the primordial power spectrum and the early expansion history of our Universe. We present a Bayesian approach aimed at reconstructing both the shape of the scalar power spectrum and the Universe's equation of state from GW observations, using interpolating splines to flexibly capture features in the GW data. The optimal number of spline nodes is chosen via Bayesian evidence, aiming at balancing complexity of the model and the fidelity of the reconstruction. We test our method using both representative mock data and recent pulsar timing array measurements, demonstrating that it can accurately reconstruct the curvature power spectrum as well as the underlying equation of state, if different from radiation.

DOI: 10.1103/n23j-5bfc

I. INTRODUCTION

The power spectrum of curvature perturbations, $\mathcal{P}_\zeta(k)$, plays a crucial role in understanding the early Universe and the formation of cosmic structure. While the cosmic microwave background (CMB) and large-scale structure of the Universe provide constraints on its features at large cosmological scales (see, e.g., [1]), smaller scales remain relatively unconstrained. One promising avenue to probe this regime is through scalar-induced gravitational waves (SIGWs), which arise as a second-order effect of primordial density perturbations: see, e.g., [2–11] for original and key papers, and [12] for a comprehensive, detailed review. Such induced gravitational waves carry valuable information about the small-scale features of $\mathcal{P}_\zeta(k)$ and may be detected by future gravitational wave observatories, such as the Laser Interferometer Space Antenna (LISA) [13] and the Einstein Telescope [14]. Enhanced scalar fluctuations, leading to observable gravitational wave (GW) signals, can be produced on models leading to primordial black holes, see, e.g., [15] for a review. In addition to encoding information about the primordial power spectrum, the GW spectrum is also sensitive to the expansion history of the Universe (see, e.g., [16–18]). This is good news since deviations from a purely radiation-dominated phase at very early times can leave distinct imprints on the shape and amplitude of the GW spectrum, which can be inferred from data. Such departures might arise from exotic physics or alternative cosmological scenarios, and they can be parametrized in terms of an effective equation of state parameter [12]. A detection of SIGWs, therefore, offers a unique opportunity not only to reconstruct $\mathcal{P}_\zeta(k)$, but also to infer the background expansion dynamics.

The formation of SIGW is a process occurring at second order in fluctuations, and it is difficult to analytically disentangle properties of the primordial sources from GW data alone. In this work, we develop an automated and efficient method to do so, based on Bayesian inference techniques. Our reconstruction framework allows also one to simultaneously determine the equation of state parameter alongside the power spectrum, aiming to uncover hints of nonstandard early Universe evolution.

In our Bayesian approach to reconstruct the power spectrum, we represent it in the form of an interpolating spline with variable number of nodes, positions and amplitudes, all to be determined from GW data. For a model with fixed number of nodes, the posterior distributions of the spline position and amplitude parameters are determined using nested sampling while the Bayesian evidence criterion is used to compare the relative probabilities of models with different numbers of nodes. To test our method, we generate mock Ω_{GW} for power spectra

---

[*] Contact author: aya-ghaleb@outlook.com
[†] Contact author: ameek.malhotra@swansea.ac.uk
[‡] Contact author: g.tasinato2208@gmail.com
[§] Contact author: e.i.zavalacarrasco@swansea.ac.uk

representative of early Universe scenarios leading to enhanced scalar perturbations and three scenarios of post-inflationary cosmological background evolution—radiation domination, early matter domination transitioning to radiation domination and a general equation of state w different from matter or radiation. For the latter, we also test the viability of our method in determining w, in addition to the curvature power spectrum. The results that we present here can be reproduced using our code available on GitHub.[1]

This paper is organized as follows. Section II reviews theory aspects of SIGW. In Sec. III we describe our method, starting from the calculation of $\Omega_{\rm GW}$ to generate our mock data and then discuss in detail the inverse problem of reconstructing $\mathcal{P}_\zeta$ from $\Omega_{\rm GW}$. Section IV presents the results of our reconstruction for representative examples as well as using recent pulsar timing array data. Section V presents our conclusions, followed by technical Appendixes.

II. INDUCED GWS AND THE UNIVERSE'S EXPANSION HISTORY

In this section we collect and outline the key equations and conventions relevant for the computation of SIGWs in different cosmological scenarios. We review three cases for the post-inflationary evolution: the standard case of radiation domination (RD) $c_s^2 = w = 1/3$ (see the review [12]), a sudden transition from an early matter-dominated (eMD) phase to RD (see, e.g., [20]), and an adiabatic perfect fluid domination with general (constant) equation of state $c_s^2 = w$ [12]. These three cases will then be analysed respectively in Secs. IV A, IV B, and IV C.

The physics of SIGWs relies on second-order effects in cosmological perturbation theory. Primordial GWs are amplified once scalar curvature perturbations originating from quantum fluctuations during inflation act as sources for tensor modes (GW) upon their horizon reentry. The detectability of the resulting gravitational wave background relies in part on the amplitude of these scalar perturbations: a sufficiently enhanced scalar power spectrum at small scales can lead to observable SIGWs in current or future gravitational wave observatories.

On large cosmological scales, such as those probed by the CMB with characteristic wave numbers $k \sim 0.001\ \mathrm{Mpc}^{-1}$, observations constrain the amplitude of scalar perturbations to be of order $\mathcal{P}_\zeta \sim 10^{-9}$ [1]. This leads to an unobservable small SIGW signal on CMB scales. At much smaller scales ($k \gg 1\ \mathrm{Mpc}^{-1}$), however, there are no direct observational bounds on $\mathcal{P}_\zeta$, allowing for the possibility of significant enhancement. In such scenarios, the induced gravitational wave spectrum can attain amplitudes within the sensitivity range of a variety of GW detectors. This opens a new observational window into the small-scale structure of the primordial Universe, complementary to CMB and large-scale structure surveys, which are sensitive to larger scales.

The energy density spectrum of SIGWs arises from a convolution over two copies of the scalar power spectrum $\mathcal{P}_\zeta$ and a transfer function $\mathcal{T}$ (also referred to as the kernel), which encodes the evolution of the tensor modes in the cosmological background. The dominant contribution is given by a double integral over momenta, weighted by these two elements.

In the standard thermal history, inflation is followed by reheating, which initiates an RD era. Scalar perturbations that exit the horizon during inflation reenter during RD and source GWs at second order. However, SIGWs are not merely sensitive to the inflationary perturbations, they also offer a probe of the Universe's postinflationary thermal history, particularly the epoch between inflation and big bang nucleosynthesis (BBN), which remains largely unconstrained by conventional observations. This period could include nonstandard cosmological phases, such as early matter domination or kination, motivated by scenarios in high-energy physics and string theory.[2]

The energy density spectrum of SIGWs takes the general form [12]

$$\Omega_{\rm GW}(\eta, k) = \frac{1}{12}\left(\frac{k}{\mathcal{H}(\eta)}\right)^2 \overline{\mathcal{P}_h(\eta, k)}, \tag{2.1}$$

where η is the conformal time, $\mathcal{H}(\eta) = a'(\eta)/a(\eta)$ the conformal Hubble parameter, and the overline denotes an average over oscillations. The induced tensor power spectrum can be written as,

$$\overline{\mathcal{P}_h(\eta, k)} = 8 \int_0^\infty \mathrm{d}v \int_{|1-v|}^{1+v} \mathrm{d}u \left(\frac{4v^2 - (1+v^2-u^2)^2}{4uv}\right)^2 \times \overline{I^2(u, v, k, \eta)}, \mathcal{P}_\zeta(ku)\mathcal{P}_\zeta(kv), \tag{2.2}$$

where $\mathcal{P}_\zeta$ is the curvature power spectrum, and

$$v \equiv \frac{q}{k}, \qquad u \equiv \frac{|\mathbf{k} - \mathbf{q}|}{k}. \tag{2.3}$$

The kernel I, defined by a convolution of the source with a Green's function, depends on the evolution of the scalar perturbations and the background cosmology,

$$I(u, v, k, \eta) = \int_{\eta_i}^{\eta} \mathrm{d}\tilde{\eta}\, G_k(\eta, \tilde{\eta}) f(u, v, k, \tilde{\eta}). \tag{2.4}$$

The exact form of this expression changes with the equation of state of the Universe, motivating us to now present the specific cases we analyze in what follows.

---

[1] [19].

[2] See [21] for a recent review on string cosmology, and [22,23] for reviews on nonstandard postinflationary histories.

(a) *Radiation domination*: This is the most well-studied case in the literature, see, e.g., [12], and corresponds to an equation of state with $w = 1/3$. The expression for the induced $\Omega_{\rm GW}$ results in

$$\Omega_{\rm GW,RD} = \int_0^\infty dv \int_{|1-v|}^{1+v} du \mathcal{T}_{\rm RD}(u, v, c_s) \times \mathcal{P}_\zeta(ku)\mathcal{P}_\zeta(kv), \tag{2.5}$$

where c_s is the propagation speed of scalar perturbations and the function $\mathcal{T}_{\rm RD}(u, v, c_s)$ is given by

$$\mathcal{T}_{\rm RD} = \frac{y^2}{3c_s^4}\left[\frac{4v^2 - (1-u^2+v^2)^2}{4u^2v^2}\right]^2 \times \left(\frac{\pi}{2}4y^2\Theta[c_s(u+v)-1] + \left(1 - \frac{1}{2}y\ln\frac{1+y}{1-y}\right)^2\right), \tag{2.6}$$

where y is defined as,

$$y = 1 - \frac{1 - c_s^2(u-v)^2}{2c_s^2 uv}. \tag{2.7}$$

In our work we compute the GW density $\Omega_{\rm GW}$ for this case using the numerical code SIGWAY [24].

(b) *Early matter domination*: We consider a scenario in which a period of eMD precedes the onset of RD, with a sudden transition between the two phases—referred to here as reheating. A distinctive feature of this setup is the sharp enhancement of the SIGW signal immediately after the transition [20]. This enhancement arises because, during eMD, the scalar source term responsible for GW production remains constant and does not efficiently generate GWs. However, the onset of radiation domination leads to efficient GW production. This characteristic imprint in the GW spectrum may fall within the sensitivity reach of upcoming observatories such as LISA, providing a unique observational window into the pre-BBN universe and the reheating dynamics.

It is important to note that this enhancement is sensitive to the details of the transition. The assumption of a *sudden transition* corresponds to a change in the background evolution occurring on a timescale much shorter than the Hubble time at reheating. In realistic scenarios, however, the transition is expected to be gradual. During such an intermediate period, the evolution of perturbations is continuous, and their behavior cannot be fully captured by either the pure eMD or RD approximations. Several studies have explored this regime using smoothed background interpolations [25–28], showing that the resulting SIGW spectrum is modified in both amplitude and shape compared to the sudden-transition limit.

As discussed in [20], assuming a sudden transition, however, remains a reasonable approximation in two key regimes: for modes with $k \ll k_{\rm rh}$, which remain superhorizon at reheating and thus have constant curvature perturbations unaffected by the nature of the transition; and for modes with $k \gg k_{\rm rh}$, which are already subhorizon and oscillating well before reheating, making their evolution similarly insensitive to how reheating proceeds. The approximation begins to fail, however, for modes with $k \sim k_{\rm rh}$, which enter the horizon around the time of reheating and are therefore more sensitive to whether the transition is sharp or gradual. That said, if the peak of the primordial power spectrum corresponds to modes that enter the horizon well before reheating, then the dominant contribution to the induced gravitational wave signal comes from earlier times. In this case, reheating does not introduce a significant new source of GWs, and only affects a narrow range of modes near $k_{\rm rh}$, which do not dominate the overall spectrum. For instance, in models with a sharp infrared (IR) cutoff at some scale $k_{\rm IR}$, where $k_{\rm IR} \gg k_{\rm rh}$, all relevant modes contributing to GW production enter the horizon before reheating. As long as the evolution of induced GWs is also correctly connected across the transition, then we can adopt this sudden transition scenario. This approach is demonstrated by numerical results such as [20,24].

The kernel entering Eq. (2.2) can be decomposed into

$$\overline{I^2(u,v,x,x_{\rm rh})} \simeq \overline{I^2_{\rm eMD}(u,v,x,x_{\rm rh})} + \overline{I^2_{\rm RD}(u,v,x,x_{\rm rh})}, \tag{2.8}$$

where as before, a subscript "rh" denotes the time of reheating and $x \equiv k\eta$. In sudden reheating scenarios, we focus on gravitational waves induced during the radiation-dominated era by scalar perturbations that previously experienced an early matter-dominated phase on subhorizon scales. While GWs can also be generated during the eMD era [29,30], their amplitude is typically much smaller than those produced during the RD era, where conditions are more favorable for GW amplification. This is particularly the case in sudden reheating scenarios [20]. Thus, we consider primarily the RD contribution, and modes with $k > k_{\rm rh}$, which experienced a nontrivial evolution before the Universe transitioned to radiation domination. The kernel is approximated in terms of two dominant contributions given in terms of the more convenient variables, s, t defined as

$$s \equiv u - v, \qquad t \equiv u + v - 1. \tag{2.9}$$

The first contribution is associated with modes deep inside the horizon, where the integral is dominated by the large scale t region (LS). In this limit, an analytical approximation is obtained by fixing $s = 0$ and integrating over t, leading to

$$\overline{I^2_{\rm RD,LS}}\big|_{s=0} \simeq \frac{9t^4 x_{\rm rh}^8 \left(4{\rm Ci}(\frac{x_{\rm rh}}{2})^2 + (\pi - 2Si(\frac{x_{\rm rh}}{2}))^2\right)}{81920000}. \tag{2.10}$$

This approximation is valid for large-scale modes with $k \ll k_{\rm cut}$, where $k_{\rm cut}$ is the scale corresponding to the onset of eMD, or the scale where density perturbations become nonlinear [20,25].

The second contribution accounts for the resonancelike peak in the spectrum (res). In this case, the integration is performed over s, while fixing $t = \sqrt{3} - 1$ throughout, except in the argument of the cosine integral function Ci, where a logarithmic singularity leads to an enhancement,

$$\overline{I^2_{\rm RD,res}} \approx Y \frac{9(-5 + s^2 + 2t + t^2)^4 x_{\rm rh}^8}{81920000(1 - s + t)^2 (1 + s + t)^2} {\rm Ci}(|y|)^2, \tag{2.11}$$

where $y \equiv (t - \sqrt{3} + 1)x_{\rm rh}/(2\sqrt{3})$ and Y is a numerical factor that absorbs the uncertainties in the integration limits. The total induced GW spectrum after reheating can be approximated as the sum of these two contributions,

$$\Omega^{\rm eMDRD}_{\rm GW,rh} \simeq \Omega^{\rm (LS)}_{\rm GW,rh} + \Omega^{\rm (res)}_{\rm GW,rh}. \tag{2.12}$$

In our work, by means of these analytical forms of the kernel, we compute the GW density $\Omega_{\rm GW}$ using the numerical code SIGWAY [24].

(c) *General* w: During a cosmological epoch characterized by a constant equation of state parameter w and a constant scalar sound speed c_s, the transition to radiation domination introduces a new characteristic scale. This scale is defined by the comoving wave number $k_{\rm rh}$, which corresponds to the mode that reentered the horizon at the onset of radiation domination.

The GW spectrum under such conditions has been studied in [16–18] (see the review [12] for a detailed discussion). We are interested in particular in the regime where all relevant modes reenter the horizon well before reheating, i.e., $k \gg k_{\rm rh}$. The kernel averaged over oscillations is given by,

$$\begin{aligned}\overline{I^2(u,v,x)} = {} & x^{-2(b+1)} 4^{2b} \Gamma^4[b + 3/2] \left(\frac{2b+3}{b+2}\right)^2 \frac{|1 - y^2|^b}{2c_s^4 u^2 v^2} \\ & \times \left\{ \left({\rm P}_b^{-b}(y) + \frac{b+2}{b+1} {\rm P}_{b+2}^{-b}(y)\right)^2 \Theta[c_s(u+v) - 1] \right. \\ & + \frac{4}{\pi^2} \left({\rm Q}_b^{-b}(y) + \frac{b+2}{b+1} {\rm Q}_{b+2}^{-b}(y)\right)^2 \Theta[c_s(u+v) - 1] \\ & \left. + \frac{4}{\pi^2} \left(\mathcal{Q}_b^{-b}(-y) + 2\frac{b+2}{b+1} \mathcal{Q}_{b+2}^{-b}(-y)\right)^2 \Theta[1 - c_s(u+v)] \right\}. \end{aligned} \tag{2.13}$$

Here, $\Theta[x]$ denotes the Heaviside step function. The functions ${\rm P}_b^{-b}(y)$ and ${\rm Q}_b^{-b}(y)$ are Ferrers functions of the first and second kind, valid for $|y| < 1$, while $\mathcal{Q}_b^{-b}(y)$ is the associated Legendre function of the second kind, used for $|y| > 1$, where y is defined as in Eq. (2.7) This parameter is geometrically related to the shape of the momentum triangle formed by the interacting modes. Finally b is related to the equation of state by,

$$b = \frac{1 - 3w}{1 + 3w}. \tag{2.14}$$

The presence of the Heaviside functions in Eq. (2.13) indicates momentum conservation.

For $k \gg k_{\rm rh}$, induced GWs are effectively free to propagate close to the reheating epoch. Therefore, it is appropriate to evaluate the GW energy density spectrum at the moment of reheating, $\eta = \eta_{\rm rh}$, as,

$$\Omega_{\rm GW}(\eta \gg \eta_{\rm rh}, k \gg k_{\rm rh}) = \frac{1}{12} \left(\frac{k}{\mathcal{H}(\eta)}\right)^2 \overline{\mathcal{P}_h(\eta, k)}\Big|_{\eta = \eta_{\rm rh}}. \tag{2.15}$$

Remembering that $x = k\eta$, setting

$$k_{\rm rh} = \mathcal{H}_{\rm rh} = \frac{1 + b}{\eta_{\rm rh}} \tag{2.16}$$

yields a scaling factor $(k/k_{\rm rh})^{-2b}$, accounting for the different redshifting behavior of GWs before radiation domination and ensuring continuity of the solution at $\eta = \eta_{\rm rh}$.

Finally, the general expression for the GW spectrum at reheating, valid for any shape of the primordial spectrum as long as $k \gg k_{\rm rh}$, is given by

$$\Omega_{\rm GW,rh} = \left(\frac{k}{k_{\rm rh}}\right)^{-2b} \int_0^\infty dv \int_{|1-v|}^{1+v} du \mathcal{T}(u,v,b,c_s)\mathcal{P}_\zeta(ku)\mathcal{P}_\zeta(kv) \tag{2.17}$$

where the transfer function is defined as

$$\begin{aligned} \mathcal{T}(u,v,w) = {} & \mathcal{N}(b,c_s)\left(\frac{4v^2-(1-u^2+v^2)^2}{4u^2v^2}\right)^2 |1-y^2|^b \\ & \times \left\{ \left(\mathrm{P}_b^{-b}(y) + \frac{b+2}{b+1}\mathrm{P}_{b+2}^{-b}(y) \right)^2 \Theta[c_s(u+v)-1] \right. \\ & + \frac{4}{\pi^2}\left(\mathrm{Q}_b^{-b}(y) + \frac{b+2}{b+1}\mathrm{Q}_{b+2}^{-b}(y) \right)^2 \Theta[c_s(u+v)-1] \\ & \left. + \frac{4}{\pi^2}\left(\mathcal{Q}_b^{-b}(-y) + 2\frac{b+2}{b+1}\mathcal{Q}_{b+2}^{-b}(-y) \right)^2 \Theta[1-c_s(u+v)] \right\}, \end{aligned} \tag{2.18}$$

with the numerical coefficient given by

$$\mathcal{N}(b,c_s) \equiv \frac{4^{2b}}{3c_s^4}\Gamma^4\left[b+\frac{3}{2}\right]\left(\frac{b+2}{2b+3}\right)^2 (1+b)^{-2(1+b)}. \tag{2.19}$$

Following the early constant-w epoch, the gravitational potential decays, and the GW spectrum will eventually become constant. So far we denoted the spectrum at this time by a subscript "rh" and now relate it to the present-day amplitude, denoted by a subscript "0," through standard cosmological evolution,

$$\Omega_{\rm GW,0} = 0.39\left(\frac{g_c}{106.75}\right)^{-1/3} \Omega_{\rm r,0}\Omega_{\rm GW,rh}, \tag{2.20}$$

where $\Omega_{\rm r,0}$ is the current radiation energy density parameter, and g_c is the effective number of relativistic degrees of freedom at $\eta = \eta_{\rm rh}$.

In our analysis, we use a modified version of the public code SIGWFast [31] to compute the spectrum $\Omega_{\rm GW}(f)$,[3] given an input curvature power spectrum, a constant equation of state w, and a transition (or reheating) scale $f_{\rm rh}$. The SIGWFast code follows the same conventions that we adopt throughout this work.[4]

III. THE RECONSTRUCTION METHOD

As reviewed in the previous section, the amplification of primordial GWs by scalar nonlinearities is a complex process. The resulting GW density $\Omega_{\rm GW}$ is typically expressed in terms of convolution integrals depending on the (square of) the curvature perturbation spectrum, as well as on transfer functions of fluctuations through distinct cosmological eras. As a consequence, it is not easy to analytically disentangle the features of the scalar sources or the cosmological expansion history from the resulting frequency dependence of the GW density. In this section, we introduce an efficient, automated method to do so, based on Bayesian inference. The corresponding codes can be found at the link in footnote 1.

A. Spline parametrization of the power spectrum

To reconstruct the primordial curvature spectrum $\mathcal{P}_\zeta(k)$ starting from GW data, we model $\log_{10}\mathcal{P}_\zeta(k)$ using splines, i.e., a piecewise linear interpolation defined by a set of nodes, $\log_{10}\{(k_i, A_i)\}_{i=1}^N$, where k_i denotes the wave number positions of the nodes and $\log_{10} A_i = \log_{10}\mathcal{P}_\zeta(k_i)$ are the corresponding amplitudes. The linear spline method provides a simple and flexible representation of the power spectrum, capturing intricate features that may hide in the

---

[3] Where we convert the wave number to frequency using $k/{\rm Mpc}^{-1} \simeq 6.5 \times 10^{14} f/{\rm Hz}$.

[4] Up to a minor redefinition of the variables u, v in terms of s, d.

data. This approach is particularly advantageous compared to fixed functional forms (e.g., power-law or broken power-law models), as it does not impose a specific shape on the power spectrum *a priori*. We now develop arguments based on Bayasian inference to select the number and position of nodes.

The placement of the nodes is not predefined, but it is treated as free parameter to be inferred from the data, ensuring that the model remains adaptable. Only the first and last node are held fixed, based on the range over which the curvature power spectrum is interpolated. This range is typically chosen to be slightly wider than the range over which the Ω_{GW} is observed.[5] The free nodes are ordered such that $k_{i-1} < k_i < k_{i+1}$, using a bijective ordering transformation that maps a set of variables in [0, 1] to an ordered set of variables in the range $[k_{\min}, k_{\max}]$ (see, e.g., [32,33]). Such transformation is characterized by a constant Jacobian, thus if we initially place flat priors on the node locations—as we do here—the ordering transform preserves this flat shape of the prior. For the power spectrum amplitudes at the node positions, we take uniform priors $\log_{10} A_i \in [-8, -1]$, unless otherwise stated.

This free-form reconstruction approach allows the data to determine the shape of the power spectrum by adjusting both the positions and amplitudes of the spline nodes. However, increasing model flexibility risks overfitting, which can be mitigated by selecting the optimal number of nodes using Bayesian evidence—naturally balancing model complexity against goodness of fit. Building on this idea, we develop a fully Bayesian framework tailored to this problem. Similar strategies have been employed to reconstruct the primordial curvature perturbations from CMB anisotropies (see, e.g., [33,34] and references therein).

B. Bayesian model selection via Bayesian evidence

Since the complexity of the model depends on the number of spline nodes, we employ Bayesian model selection to determine the optimal number of nodes, denoted with N. In Bayesian inference, model comparison is performed using the Bayesian evidence (also known as the marginal likelihood), given by

$$\mathcal{Z}(\mathcal{M}) = \int \mathcal{L}(d|\theta, \mathcal{M}) \pi(\theta|\mathcal{M}) d\theta, \qquad (3.1)$$

where $\mathcal{L}(d|\theta, \mathcal{M})$ is the likelihood of the data d given the parameters θ and model $\mathcal{M}$, and $\pi(\theta|\mathcal{M})$ is the prior distribution of the model parameters [35]. Thus, for each spline model, the parameters θ over which we integrate are the spline node locations $\log_{10} k_i$, and the corresponding amplitudes $\log_{10} A_i$ of the scalar spectrum.

The Bayesian evidence automatically incorporates a penalty for excessive model complexity, effectively implementing Occam's razor. In fact, a model with too many spline nodes has a larger parameter space to integrate over, diluting the integral and leading to a lower evidence *unless* the additional complexity is justified by the data. By comparing $\mathcal{Z}$ across different values of N, we select the models that best balance flexibility and predictive power. Typically, differences of $\Delta \log \mathcal{Z} \gtrsim 5$ between two models (1,2) suggests that model (1) is decisively favored over model (2), with $\Delta \log \mathcal{Z}_{(12)} = \log \mathcal{Z}_{(1)} - \log \mathcal{Z}_{(2)}$, while smaller differences ($\Delta \log \mathcal{Z} \lesssim 1$) are considered to be inconclusive in terms of Jeffrey's scale [35].

The posterior distribution for the spline parameters can be highly complex, featuring multiple local maxima, as well as strong parameter degeneracies. Traditional sampling methods such as Markov chain Monte Carlo (MCMC) struggle in such cases due to the difficulty of efficiently exploring the high-dimensional space. Additionally, local optimization methods are inadequate because they can become trapped in local extrema. For the same reasons, we opt not to use Akaike information criterion or other frequentist criteria for model comparison. To overcome these challenges, we employ nested sampling [36], a particularly well-suited approach for computing Bayesian evidence while also generating posterior samples as a byproduct.

Nested sampling generates an estimate of the integral in Eq. (3.1) by reducing the integration space, focusing on the equivalent one-dimensional integral

$$\mathcal{Z} = \int \mathcal{L}(X) dX, \qquad (3.2)$$

where X is a prior volume corresponding to the likelihood $\bar{\mathcal{L}}$, defined as

$$X(\bar{\mathcal{L}}) = \int_{\mathcal{L}(\theta) > \bar{\mathcal{L}}} \pi(\theta) d\theta. \qquad (3.3)$$

Hence, $\bar{\mathcal{L}}$ can be thought of as the enclosing likelihood of cumulative prior mass X which encompasses the region where the likelihood is larger than a threshold $\bar{\mathcal{L}}$. The core algorithm begins with a set of points drawn from the prior, called live points. At each step of the algorithm, the live point with the lowest likelihood is replaced by sampling from the prior, subject to the constraint that the likelihood at the new point must be larger than the current lowest likelihood value, and a statistical estimate of the prior mass X is calculated. At the end of this process, we are left with a set of samples $\{\mathcal{L}, X\}$ which can be used to estimate the evidence as well as approximate the posterior distribution of the parameters θ [37,38]. This method has several advantages over MCMC: in addition to providing an estimate of the evidence, it can efficiently handle multimodal posteriors, and a complex posterior geometry.

---

[5] In our analysis, we find taking $k_{\min} = 10 k_{\min,\mathrm{GW}}$ and $k_{\max} = 10 k_{\max,\mathrm{GW}}$ to work well for most examples.

We implement nested sampling using the publicly available libraries PolyChord [39,40] and Nautilus [41].

C. Functional posteriors

After obtaining posterior samples for the node parameters, we visualize the reconstructed power spectrum using functional posterior plotting. For a given model, instead of plotting individual samples or posterior distributions for the spline node locations and amplitudes—which can be difficult to interpret—we use the distribution of the sampled node locations and amplitudes to estimate the probability distribution of $\mathcal{P}_\zeta$ and $\Omega_{\rm GW}$ at each wave number (or frequency). As an example, the mean of the power spectrum amplitude at a given value of k can be written as

$$\mathbb{E}[\mathcal{P}_{\zeta,k}|\mathcal{M}] = \int d\theta\, \mathcal{P}_{\zeta,k}(\theta,\mathcal{M}) p(\theta|d,\mathcal{M}), \tag{3.4}$$

where $\mathcal{P}_{\zeta,k}(\theta,\mathcal{M})$ denotes the power spectrum amplitude at a wave number k for the node locations and amplitudes under the spline model $\mathcal{M}$, while $p(\theta|d,\mathcal{M})$ is the posterior distribution of the spline parameters under the model $\mathcal{M}$.

In the spirit of Bayesian inference, we further marginalize over all the models with a different number of nodes, using the evidence ratios as the weights for the marginalization. Following such a procedure, the above estimate of the mean—taken over all the models with different number of nodes n—can then be expressed as

$$\mathbb{E}[\mathcal{P}_{\zeta,k}] = \frac{\sum_n \mathbb{E}[\mathcal{P}_{\zeta,k}|\mathcal{M}_n]\mathcal{Z}_n}{\sum_n \mathcal{Z}_n}. \tag{3.5}$$

Similarly, for each frequency bin in momentum k (or frequency f)-space, we can compute other summary statistics such as the median and credible intervals for $\mathcal{P}_\zeta$ and $\Omega_{\rm GW}$ from the posterior samples.

IV. RESULTS

We present results for selected representative cases, showing the functional posterior distributions of $\mathcal{P}_\zeta$ and $\Omega_{\rm GW}$ when marginalized over models with varying numbers of spline nodes. We also include a plot of the Bayes factor $\log\mathcal{Z}$ as a function of the number of nodes used in the reconstruction of $\mathcal{P}_\zeta$. Unless otherwise stated, for each of the $\Omega_{\rm GW}$ spectra considered we generate 1σ error bars for the observed $\Omega_{\rm GW}$ values at 50 logarithmically spaced frequencies in $5\times10^{-5}[{\rm Hz}] < f < 10^{-2}[{\rm Hz}]$ with

$$\Delta\Omega_{\rm GW}(f) = \Omega_{\rm GW,obs}(f)[0.1 + 0.05(\log f/f_*)^2]. \tag{4.1}$$

As an example, we choose the pivot frequency $f_* = 10^{-3}$ Hz as representative for LISA, with low uncertainties around the peak sensitivity f_* and increasing ones toward the two ends of LISA's sensitivity range (see, e.g., [13]). We then use the result to create a Gaussian likelihood for the $\Omega_{\rm GW}$ as an input for the nested sampler, i.e.,

$$-2\ln\mathcal{L} = \sum_f \left(\frac{\Omega_{\rm GW,model} - \Omega_{\rm GW,obs}}{\Delta\Omega_{\rm GW}}\right)^2. \tag{4.2}$$

In our analysis, we assume that such $\Omega_{\rm GW}$ spectrum is reconstructed from detector data—e.g., using codes such as SGWBinner [42,43] in the case of LISA (see also [44–46])—thus providing datasets consisting of the observed values of $\Omega_{\rm GW}$ and their associated uncertainties $\Delta\Omega_{\rm GW}$, over certain frequency ranges specific to the instruments.[6]

While the spectra and error bars are highly idealized, and artificially generated with LISA as a representative experiment to keep in mind, the methods we present do not rely on this being the case. They are applicable for any general form for $\Omega_{\rm GW}$ and any GW experiment. In particular, one may consider more realistic realizations of the $\Omega_{\rm GW}$ data simulated using the LISA noise model, without changing our method.[7] We should note though that the curvature spectrum reconstruction can only be as good as the $\Omega_{\rm GW}$ reconstruction from detector data.

A. Standard radiation domination

We start discussing our results in the framework of standard cosmological expansion, in which radiation domination directly follows the inflationary epoch. In this case, the transfer function is given by Eq. (2.6) and $\Omega_{\rm GW,rh}$ in Eq. (2.5) is understood to be evaluated at the time when the source terms have sufficiently decayed, after which the induced tensor perturbations evolve as freely propagating gravitational waves. We present reconstruction results for the three distinct scalar spectrum templates shown in Fig. 1. In each case, the scalar spectral shape is held fixed (upper panel), and we attempt to reconstruct it from the induced gravitational wave signal it gives rise to (lower panel). In Appendix A we test our method against recent pulsar timing array measurements.

1. Broken power law

We start considering a broken power law (BPL) template shown in the left panel of Fig. 1 (see, e.g., [47–49]),

---

[6] This assumption helps us to focus our attention entirely on our reconstruction method but is not a necessity. This reconstruction method (or any other) can be easily incorporated into existing codes in such a manner that eliminates the need for a separate initial inference step to obtain $\Omega_{\rm GW}, \Delta\Omega_{\rm GW}$. However, the two-step procedure has the advantage that the reconstruction method need not be applied repeatedly to the full dataset, but only to the $\Omega_{\rm GW}$ data, making it computationally more feasible.

[7] In Appendix C we also present results for noisy realizations of the $\Omega_{\rm GW}$ data.

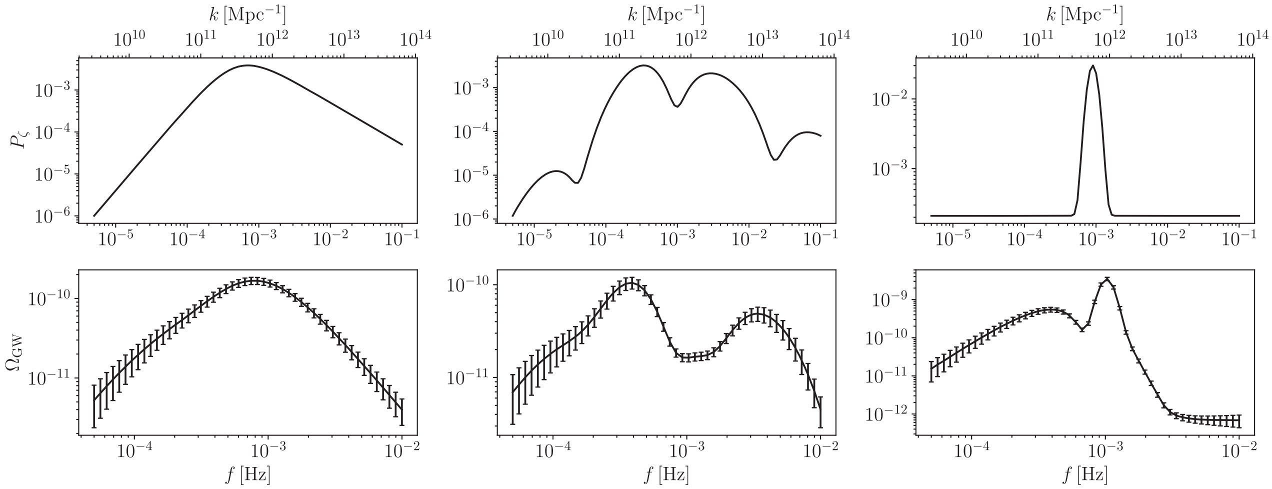

FIG. 1. Test spectra chosen for power spectrum reconstruction assuming radiation domination. *First column*: $\mathcal{P}_\zeta$ and Ω_{GW} for the broken power law profile of Sec. IV A 1. *Second column*: $\mathcal{P}_\zeta$ and Ω_{GW} for the template with oscillatory features of Sec. IV A 2. *Third column*: $\mathcal{P}_\zeta$ and Ω_{GW} for the peaked profile of Sec. IV A 3. For each column in the second row, we also show the corresponding error bars on Ω_{GW}, as dictated by Eq. (4.1).

$$\mathcal{P}_\zeta(f) = A\left(\frac{f}{f_*}\right)^{n_{\mathrm{IR}}}\left(1+\left(\frac{f}{f_*}\right)^{\sigma}\right)^{\frac{n_{\mathrm{UV}}-n_{\mathrm{IR}}}{\sigma}}, \qquad (4.3)$$

where A is the amplitude, f_* a reference frequency, $n_{\mathrm{IR,UV}}$ the spectral indexes in the infrared and ultraviolet part of the spectrum, while σ is a parameter controlling the smoothness of the transition.

To start with, we fix the parameter values of Eq. (4.3) as

$$A = 10^{-2}, \qquad f_* = 5\times10^{-4}\ \mathrm{Hz}, \qquad n_{\mathrm{IR}} = 2,$$
$$n_{\mathrm{UV}} = -1, \quad \sigma = 2, \qquad (4.4)$$

to ensure that the peak of the induced GW spectrum lies in the middle of the LISA band.

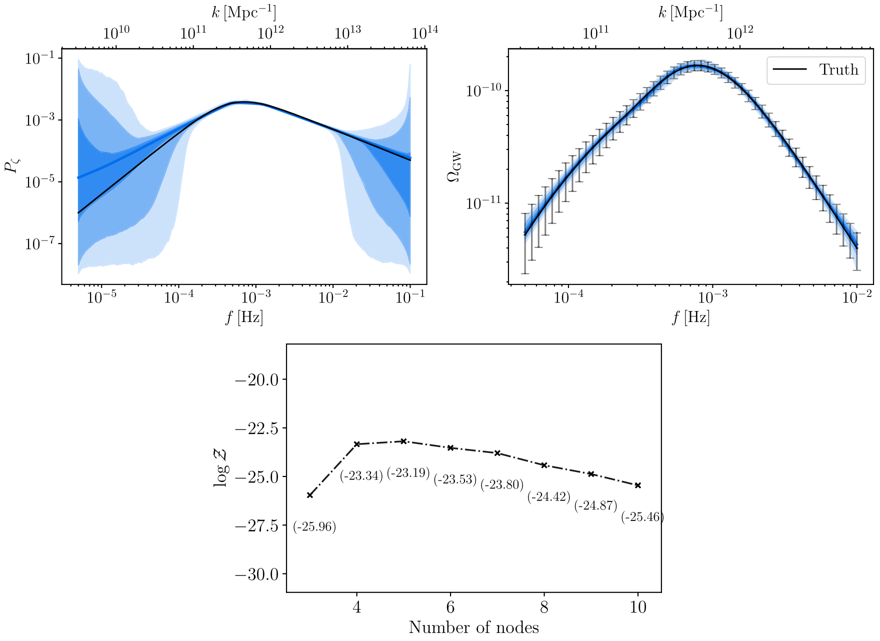

FIG. 2. *Top*: The reconstructed $\mathcal{P}_\zeta$ and Ω_{GW} for the BPL model of Sec. IV A 1, with parameters as in Eq. (4.4) marginalized over the models with different number of nodes. The different shaded regions correspond to 68%, 95% and 99.7% credible intervals for $\mathcal{P}_\zeta$ and Ω_{GW}. *Bottom*: The evidence $\log\mathcal{Z}$ as a function of the number of nodes.

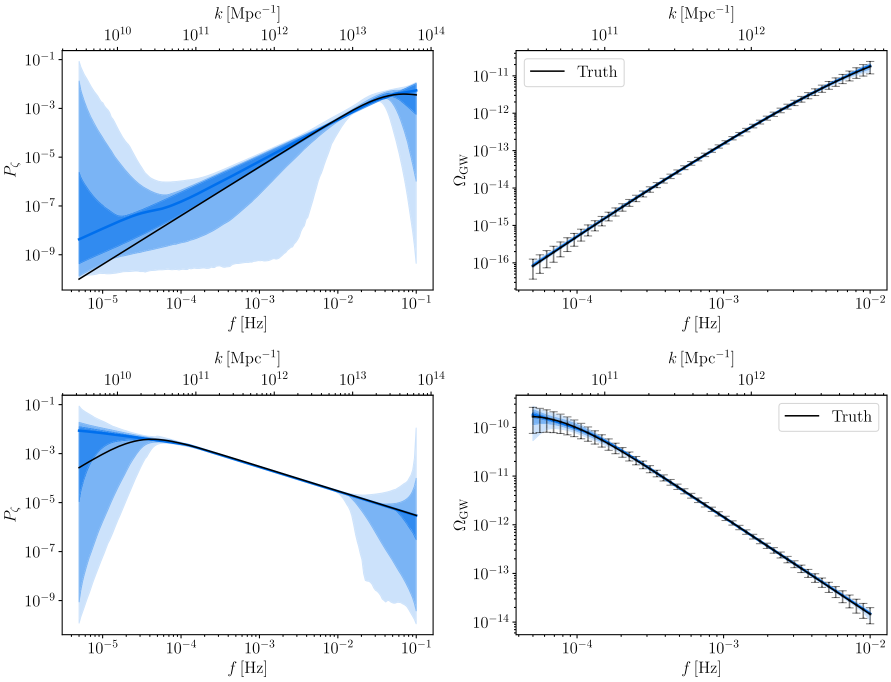

FIG. 3. Reconstruction of the BPL power spectrum using if only the IR (top) and UV (bottom) part of the spectrum were observed by the experiment. The different shaded regions correspond to 68%, 95% and 99.7% credible intervals for $\mathcal{P}_\zeta$ and Ω_GW.

Our results are shown in Fig. 2. The Bayesian evidence here favors the $N = 4, 5$ model the most and decreases as we increase the number of nodes, suggesting that the shape of the spectrum can be captured sufficiently well with four and five nodes.[8]

We find that the scalar power spectrum $\mathcal{P}_\zeta$ can be accurately reconstructed near the peak, while larger uncertainties appear at the edges, reflecting the limitations of the input data. In particular, the constraints on the power spectrum in the infrared (IR) are almost entirely prior dominated. This is due to two key reasons: (i) IR modes far from the peak contribute negligibly to the SIGW spectrum around the peak, and (ii) the IR tail of the SIGW spectrum generated during radiation domination exhibits a universal k^3 behavior, up to logarithmic corrections (see, e.g., [12,48,50–53]). Nevertheless, it is known that in single field inflation $\mathcal{P}_\zeta$ can not normally growth steeper than k^4 in the infrared [54,55] (but see, e.g., [56–59] for exceptions).

As a second case, we assume that only the UV or IR portion of the spectrum is detected by the experiment. We use the same parameters as the original BPL example, except for $f_* = 3 \times 10^{-5}, 5 \times 10^{-2}$ Hz, for the UV and IR cases respectively. The corresponding results are shown in Fig. 3. In the IR, the universal k^3 scaling of the Ω_GW spectrum far from the peak implies that $\mathcal{P}_\zeta$ cannot be reliably reconstructed in the tails, where the constraints are almost entirely prior dominated. In contrast, the UV tail of the Ω_GW spectrum is sensitive to the UV tilt of the curvature power spectrum, hence enabling its reconstruction.[9] These results can be understood analytically by noting that if n_IR and n_UV denote the IR and UV tilts of the curvature power spectrum, then the induced Ω_GW spectrum exhibits the following asymptotic behavior (see, e.g., [12]):

$$\Omega_\mathrm{GW}(k) \propto \begin{cases} \left(\frac{k}{k_\mathrm{p}}\right)^3, & k \ll k_\mathrm{p}, \\ \left(\frac{k}{k_\mathrm{p}}\right)^{-\Delta}, & k \gg k_\mathrm{p}, \end{cases} \quad \text{with}$$
$$\Delta = \begin{cases} 2n_\mathrm{UV}, & 0 < n_\mathrm{UV} < 4, \\ 4 + n_\mathrm{UV}, & n_\mathrm{UV} > 4, \end{cases} \tag{4.5}$$

where k_p is the peak scale. It is clear from the above equations that for such BPL profiles of the curvature power spectrum, the IR tilt plays no role in the shape of the SIGW spectrum whereas the UV tilt does. This is very much reflected in the marginalized posteriors of the curvature power spectrum for the all the examples seen previously.

---

[8] Nested sampling produces a statistical estimate of $\log \mathcal{Z}$, thus these numbers in Fig. 2 come with their associated uncertainties. When running Nautilus to sample the posterior and compute the evidence, we choose settings to ensure that the resulting uncertainty is small $\Delta \log \mathcal{Z} < 0.1$ (see [41] and also Nautilus FAQs) Since this is much smaller compared to the range over which $\log \mathcal{Z}$ varies as a function of the number of nodes, we do not show it in the plots.

[9] We noticed a similar behavior for additional radiation-dominated examples we explored.

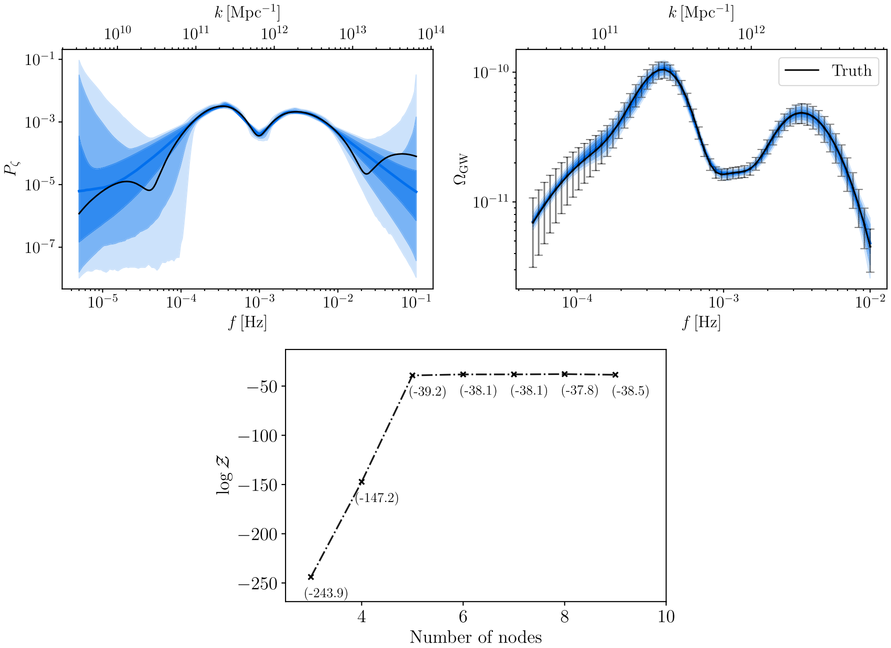

FIG. 4. *Top*: The reconstructed $\mathcal{P}_\zeta$ and $\Omega_{\rm GW}$ for the oscillatory model of Eq. (4.6), marginalized over the models with different number of nodes. See Sec. IV A 2. The different shaded regions correspond to 68%, 95% and 99.7% credible intervals for $\mathcal{P}_\zeta$ and $\Omega_{\rm GW}$. *Bottom*: The evidence $\log \mathcal{Z}$ as a function of the number of nodes.

2. A template with oscillatory features

As a second representative template for the curvature power spectrum, we modify the BPL profile (4.3) including oscillatory features (middle column, Fig. 1. See, e.g., [24,60–62] for physical motivations)

$$\mathcal{P}_\zeta(f) = A \cdot \left(\frac{f}{f_*}\right)^{n_{\rm IR}} \cdot \left(1 + \left(\frac{f}{f_*}\right)^{\sigma}\right)^{\frac{n_{\rm UV}-n_{\rm IR}}{\sigma}} \times (1 + B\cos((\ln f/C)^2)). \qquad (4.6)$$

The new parameters A, B, C control the oscillations. We fix their values $A = 10^{-3}, B = 15, C = 2.5$ while the other parameters of Eq. (4.6) have the same values as their BPL counterparts in Eq. (4.4). The corresponding results are represented in Fig. 4. The plot indicates that our Bayesian method is able to recover the shape of the oscillations quite well. Once again, the constraints in the tails are much weaker, especially in the IR since the IR part of the $\mathcal{P}_\zeta$ spectrum contributes very little to the SIGW spectrum for peaked $\mathcal{P}_\zeta$ spectra.

3. A sharply peaked spectrum

We next try to reconstruct a curvature spectrum characterized by a sharp feature, described by a modified log-normal profile[10] (right column, Fig. 1),

$$\mathcal{P}_\zeta(f) = A \cdot \left(B + \exp\left(-\frac{1}{2}\left(\frac{\ln(f/f^*)}{C}\right)^2\right)\right). \qquad (4.7)$$

We select the parameters as $A = 3 \times 10^{-2}, B = 7 \times 10^{-3}$, $f_* = 9 \times 10^{-4}$ Hz, $C = 0.15$, so to ensure that the corresponding GW spectrum is enhanced in the LISA band. The results for this example are plotted in Fig. 5. Notice that the position and features of the peak of the curvature spectrum are reconstructed extremely well since the resonant peak and dips in the SIGW spectrum are highly dependent on the location of the peak in the $\mathcal{P}_\zeta$ spectrum.

4. Nondetection

Finally, we present results for the case of a nondetection in Fig. 6, where we only have upper limits on the $\Omega_{\rm GW}$ over a given frequency range. For a given detector, the upper limits on $\Omega_{\rm GW}$ would be the strongest around the peak sensitivity of the detector and weaker toward the ends, which is reflected in our mock upper limits shown in Fig. 6. Since there is no detection in this case, we fix the number of nodes to four for simplicity although one can again obtain upper limits marginalized over models with different number of spline nodes as done in the previous examples. Our results demonstrate that this reconstruction method can also be applied to obtain upper limits on $\mathcal{P}_\zeta$ over a given frequency/wave number range which can complement the limits on $\mathcal{P}_\zeta$ obtained from primordial black holes (PBH) constraints. Given the exponential sensitivity of the PBH abundance to the perturbation amplitude [63], such limits can be very powerful in constraining the fraction of dark matter in PBH.

---

[10] Log-normal scalar profiles have been much explored in the recent literature. See, e.g., [24] for motivations and examples.

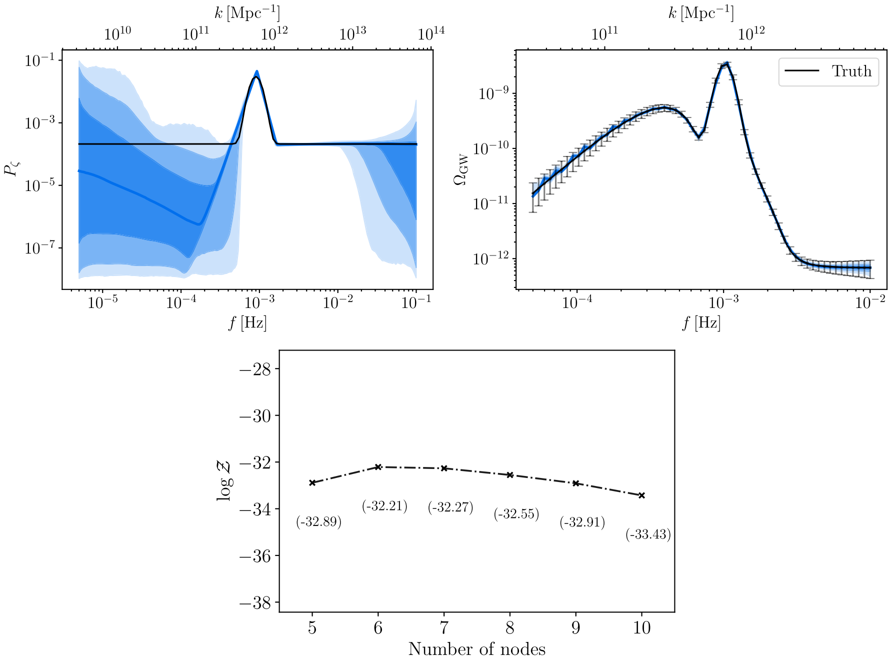

FIG. 5. *Top*: The reconstructed $\mathcal{P}_\zeta$ and $\Omega_{\rm GW}$ for the peaked model of Eq. (4.1.3) marginalized over the models with different number of nodes. See Sec. IV A 3. The different shaded regions correspond to 68%, 95% and 99.7% credible intervals for $\mathcal{P}_\zeta$ and $\Omega_{\rm GW}$. *Bottom*: The evidence $\log \mathcal{Z}$ as a function of the number of nodes.

B. Early matter domination-radiation transition

In the previous section we focused on scenarios where primordial GWs are amplified during radiation domination upon reentering the horizon. In this section and the next, we introduce an additional layer of complexity by considering cases where the Universe is not necessarily radiation dominated at the time of GW formation. In particular, we consider a cosmological scenario in which inflation is followed by a period of matter domination that transitions quickly to RD, as laid out in Sec. II. Such an eMD epoch is characterized by an equation of state parameter $w = 0$, and we impose the relation $c_s^2 = w$ for the fluid sound speed [64].

Scenarios involving an eMD phase have gained increasing attention in recent years due to their potential to enhance the amplitude of induced GWs, bringing the resulting GW signal within the sensitivity range of future detectors such as LISA, offering a potential observational probe of the thermal evolution of the Universe.

To calculate the induced GWs, we impose an abrupt cutoff on the power spectrum of curvature perturbations at $k_{\rm cut}$ which may be interpreted as the scale corresponding to the onset of eMD, or the scale where density perturbations become nonlinear $k_{\rm cut} \sim 470/\eta_{\rm rh}$ [20],

$$\mathcal{P}_\zeta(k) = 0 \quad \text{for } k > k_{\rm cut}. \tag{4.8}$$

Our aim is to evaluate whether our Bayesian reconstruction method remains accurate and well behaved in the presence of the reheating transition described above.

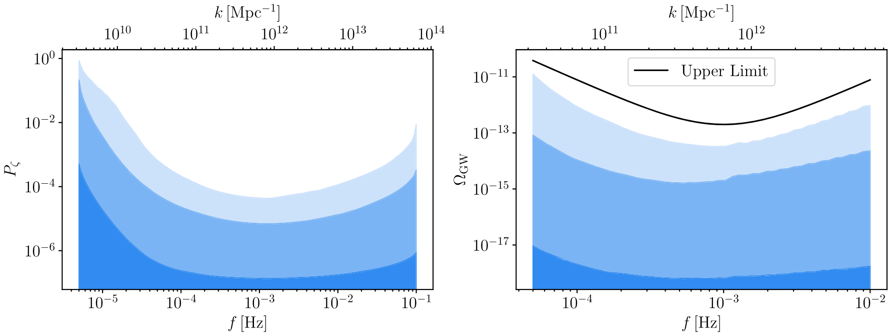

FIG. 6. Upper limits for $\mathcal{P}_\zeta$ reconstructed using four nodes from the upper limit on $\Omega_{\rm GW}$. The boundaries of the different shaded regions correspond to 68%, 95% and 99.7% upper limits. See Sec. IV A 4.

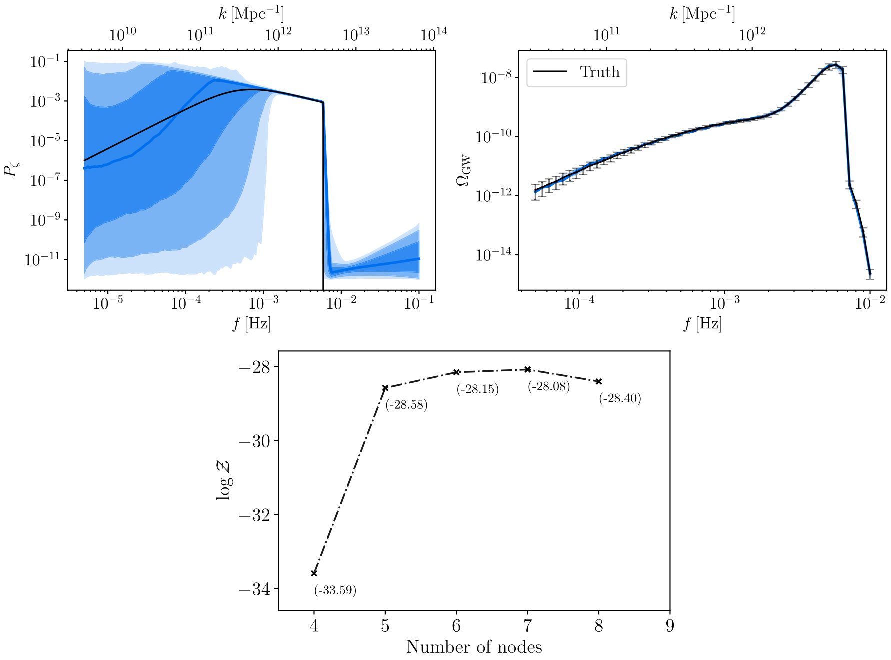

FIG. 7. *Top*: Reconstructed $\mathcal{P}_\zeta$ and $\Omega_{\rm GW}$ for the BPL model, assuming early matter domination, marginalized over the models with different number of nodes. See Sec. IV. B. The different shaded regions correspond to 68%, 95% and 99.7% credible intervals for $\mathcal{P}_\zeta$ and $\Omega_{\rm GW}$. *Bottom*: The evidence $\log \mathcal{Z}$ as a function of the number of nodes.

To this end, we adopt the following benchmark parameters:

$$\eta_{\rm rh} = 2500\ \mathrm{s}, \qquad k_{\rm cut} = 0.008\ \mathrm{s}^{-1}. \tag{4.9}$$

To further test the reconstruction capabilities of our method, we move beyond the standard assumption of a scale-invariant spectrum and consider two representative templates for $\mathcal{P}_\zeta$: the broken power-law profile of Sec. IV A 1, and the narrow peak profile of Sec. IV A 3 (see Fig. 1).

The results for the BPL model with an eMD-to-RD transition are shown in Fig. 7. The reconstruction successfully recovers the shape and amplitude of the power spectrum near the peak and around the cutoff. Larger uncertainties appear at lower frequencies, which are largely prior-dominated, and reflect the limited constraining power of the stochastic GW background in the infrared regime. At high frequencies, uncertainties arise from the shape of the resonance contribution to the GW kernel, which is sharply peaked around the transition, and results quite sensitive to the choice of reheating time.

Considering the narrow-peaked spectrum of Fig. 8, the reconstruction recovers the location and amplitude of the peak with good accuracy, hence demonstrating its sensitivity to sharply localized features in the power spectrum. As with the BPL case of Sec. IV. A. 1, we find uncertainties in the reconstruction of the infrared part, where the induced GW spectrum becomes less constraining and the reconstruction becomes increasingly prior dominated.

Proceeding with additional tests, we perform for comparison a reconstruction assuming a pure radiation-dominated background using GW data generated under an early matter-dominated to radiation-dominated (eMD-RD) scenario for the BPL model. As shown in Fig. 9, a resonance peak arising from the sudden reheating transition acts as a distinguishing feature between the two scenarios, with the Bayes factor decisively favoring the eMD-RD model. This indicates that, in principle, GW observations can be used to infer features of the transition. However, the enhancement in induced GWs is sensitive to the dynamics of the reheating process. While a sudden transition can lead to a pronounced enhancement, more gradual reheating, such as in models with constant decay rates [25] can suppress the signal, potentially weakening the apparent model preference. However, if the decay rate evolves in time, such that the field decays much more rapidly than the Hubble expansion rate at the time of transition, the induced GWs can still be significantly enhanced [65]. Thus, whether a bias in model reconstruction persists depends on the specific details of the transition dynamics, and further study is needed to assess the robustness of these conclusions across various reheating scenarios.

Additionally, it would be particularly interesting to explore whether the time dependence of the gravitational potential and its decay rate could be reconstructed from the GW signal itself. If this is feasible, it could provide insights into the underlying physics and thermal history, potentially allowing us to pinpoint key features such as

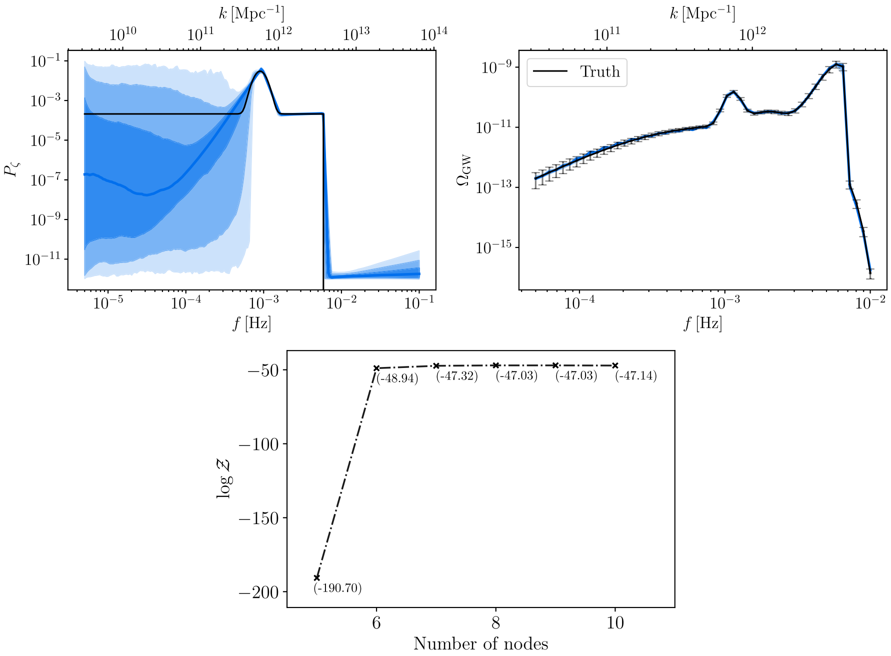

FIG. 8. *Top*: The reconstructed $\mathcal{P}_\zeta$ and $\Omega_{\rm GW}$ for the peaked model in eMD, marginalized over the models with different number of nodes. *Bottom*: The evidence log $\mathcal{Z}$ as a function of the number of nodes.

(a) the onset of the eMD era, (b) its duration, and (c) the timescale of the transition to RD. Recent studies have begun to map the impact of these factors on $\Omega_{\rm GW}$ [20,25,65,66], and using the reconstruction methods proposed in this work, it might even be possible to directly infer this information from real signals, such as those detectable by LISA, offering a direct observational probe into the thermal history of the early Universe, and

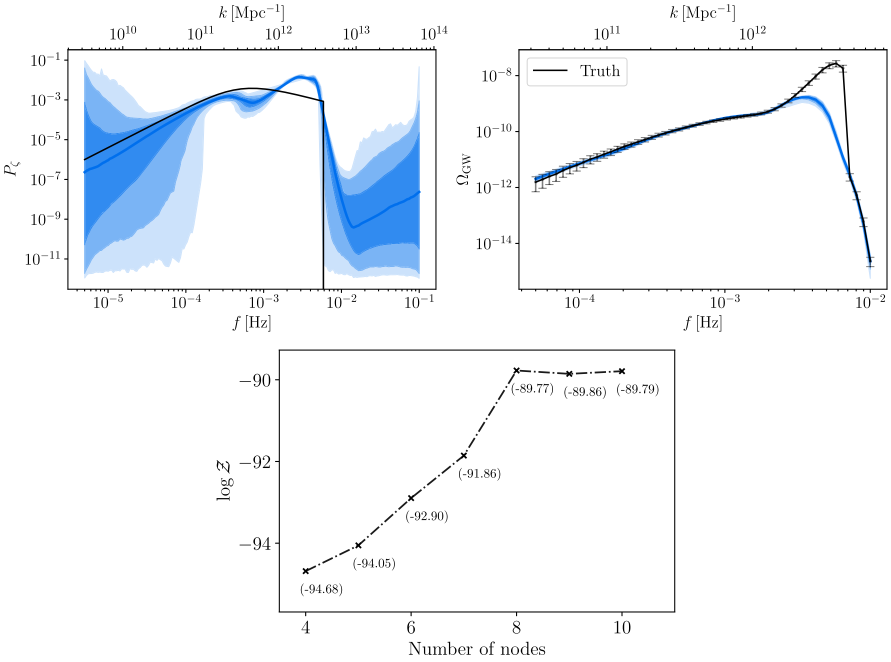

FIG. 9. *Top*: The reconstructed $\mathcal{P}_\zeta$ and $\Omega_{\rm GW}$ for the BPL model assuming eMD domination, with a run assuming RD for the same GWB data, and marginalized over the models with different number of nodes. The different shaded regions correspond to 68%, 95% and 99.7% credible intervals for $\mathcal{P}_\zeta$ and $\Omega_{\rm GW}$. *Bottom*: The evidence log $\mathcal{Z}$ as a function of the number of nodes.

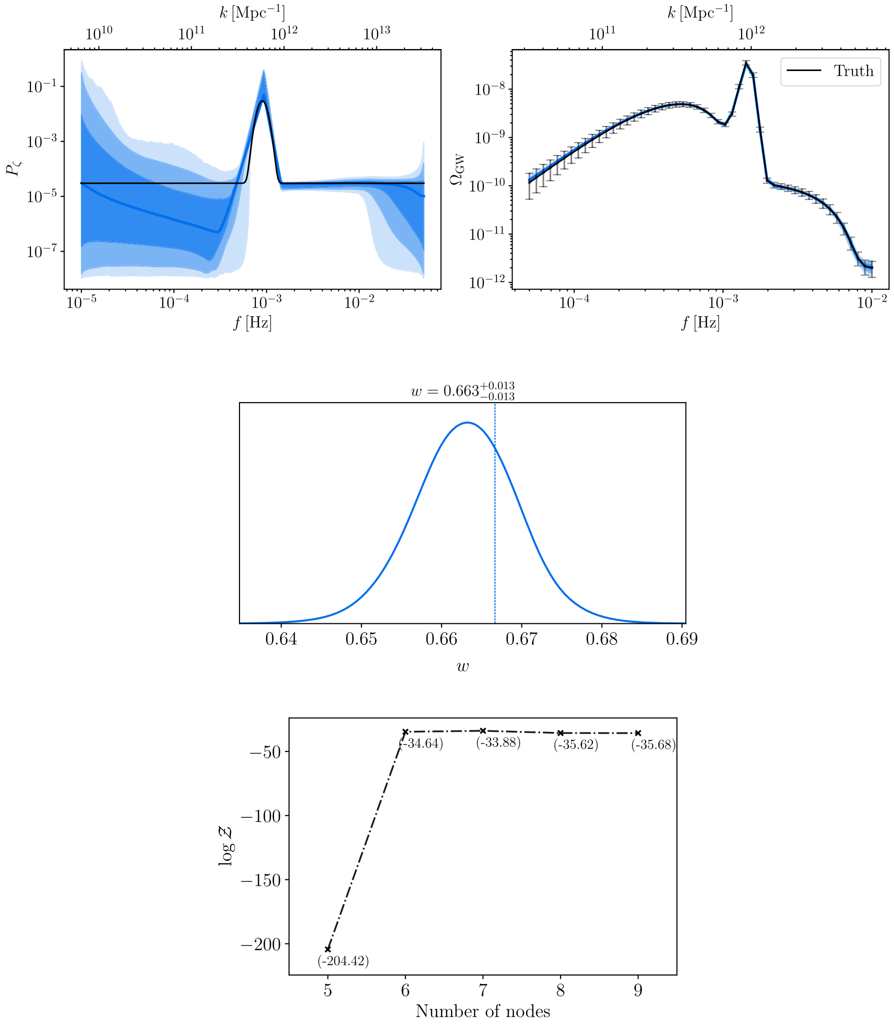

FIG. 10. Reconstruction of the peaked spectrum using linear interpolation for SIGW generated during an epoch with $w = 2/3$, see Sec. IV C. The different shaded regions correspond to 68%, 95% and 99.7% credible intervals for $\mathcal{P}_\zeta$ and Ω_{GW}. Reported limits represent to 95% credible intervals for the parameter w.

possibly also the QCD transition (see, e.g., [67,68]). We leave these considerations for future study.

C. General equation of state

We now consider the more general case in which the equation of state of the dominant fluid at the time of horizon reentry of the scalar modes can in principle differ from that of matter or radiation.

The transfer function $\mathcal{T}_w$ is given by Eq. (2.18) [12]. Our aim in this case is to use GW data not only for reconstructing the momentum shape of the primordial power spectrum, but also the equation of state w (we fix the sound speed such that $w = c_s^2$, i.e., treating this component as a perfect fluid). We make use of a modified version of the public code SIGWFast [31] to obtain the $\Omega_{\mathrm{GW}}(f)$ spectrum given an input curvature power spectrum, equation of state w and transition/reheating scale f_{rh}. SIGWFast calculates $\Omega_{\mathrm{GW}}(f)$ under the assumptions stated above (we take $f_{\mathrm{rh}} = 10^{-5}$ Hz).[11] We do not sample f_{rh} since it appears as an overall scaling factor in $\Omega_{\mathrm{GW}}(f)$, thus it is completely degenerate with the power spectrum amplitude. We leave an analysis of how f_{rh} could also be inferred by breaking this degeneracy, e.g., by additional theory motivated priors for f_{rh} or by requiring that the power spectrum does not overproduce PBH, to future studies. We present the results for our fiducial model, which has the peaked and BPL templates of Secs. IV A 3 and IV A 1 as underlying curvature power spectra, while we choose $w = 2/3$ as fiducial value for the equation of state. We use the same priors on the node amplitude and locations as in Sec. IV. A while for the equation of state we take $w \in [0, 1]$.

---

[11] Note that the code can only compute $\Omega_{\mathrm{GW}}(f)$ for $f > f_{\mathrm{rh}}$.

In Fig. 10 we plot the results for the case of peaked spectrum. We notice that the underlying curvature power spectrum as well as the equation of state can be recovered quite well. The reason of such good reconstruction is that for sharply peaked spectra, the position of the resonance peaks and dips in the SIGW spectra is strongly sensitive to the equation of state w. Thus, w is recovered not only without any significant bias but also with tiny uncertainties.

In Fig. 11, we plot our results for our BPL model. Contrary to the previous examples, for this particular example we use Gaussian process (GP) interpolation to represent the power spectrum.[12]

In addition to the positions of the nodes and their amplitudes, GP interpolation requires the specification of a kernel function K. We adopt a radial basis function as the choice for the kernel,

$$K(x,x') = \exp\left[-\frac{(x-x')^2}{2l^2}\right], \tag{4.10}$$

where x and x' denote the positions of the nodes,[13] once again in $\log_{10} k$ space and l corresponds to the GP length scale, which controls the correlation length of the GP predictions. Given positions of nodes X and amplitudes Y, the prediction of the GP interpolation at a point x_* is [69]

$$f(x_*|X,Y) = K(x_*,X)\cdot[K(X,X)+\sigma_n^2 I]^{-1}\cdot Y. \tag{4.11}$$

The term $\sigma_n^2 I$ is a small number, added to the diagonal of the GP kernel matrix $K(X,X)$ to ensure numerical stability. The GP prediction is a weighted mean of the values at the node locations, with the weights controlled by the GP length scale—longer length scales means that nodes far from the point x_* also contribute significantly to the prediction, and vice versa. We keep the same priors on the node locations and amplitudes as in the linear interpolation examples. For the length scale, the prior reads $l\in[\Delta\log_{10}k/(8\times n), \Delta\log_{10}k]$ where $\Delta\log_{10}k$ is the width of the interval (in $\log_{10}k$ space) over which $\mathcal{P}_\zeta$ is reconstructed and n is the number of nodes. This length scale prior ensures smoothness of the interpolation while not being overly restrictive. Following this procedure, we obtain that both the primordial power spectrum as well as the equation of state are recovered fairly well—see Fig. 11. However, we have larger uncertainties in the inferred w as opposed to the sharply peaked case of Fig. 10. This is due to the fact that due to the broad shape of the peak in $\mathcal{P}_\zeta$, the resonant peaks in $\Omega_{\rm GW}$ are absent. The previous discussion of Sec. IV. A. 1 with respect to the behavior of the IR and UV tails also applies here, with only slight differences: Eq. (4.5) now changes to [12]

$$\Omega_{\rm GW}(k) \propto \begin{cases} \left(\frac{k}{k_{\rm p}}\right)^3, & k \ll k_{\rm rh}, \\ \left(\frac{k}{k_{\rm p}}\right)^{3-2|b|}, & k_{\rm rh} \ll k \ll k_{\rm p}, \quad \text{with} \\ \left(\frac{k}{k_{\rm p}}\right)^{-\Delta-2|b|}, & k \gg k_{\rm p}, \end{cases}$$
$$\Delta = \begin{cases} 2n_{\rm UV}, & 0 < n_{\rm UV}+b < 4, \\ 4+n_{\rm UV}, & n_{\rm UV}+b > 4, \end{cases} \tag{4.12}$$

where $k_{\rm p}$ is the peak scale.

V. CONCLUSIONS

SIGWs produced in the early Universe carry the imprints of the underlying curvature power spectrum as well as the cosmological background dynamics at the time of GW production. Since the production of SIGW is a process occurring at second order in fluctuations, it is not easy to infer properties of the source from measurements of the GW spectrum. In this work we have explored a Bayesian approach to reconstruct the power spectrum of the primordial curvature perturbation as well the equation of state from observations of SIGW. Our method is based on using interpolating splines to represent the scalar power spectrum, with the number of nodes of the interpolation as well as their positions and amplitudes as parameters to be inferred from the data.

We applied our method to specific mock $\Omega_{\rm GW}$ data, generated to be representative of the different kinds of shapes of the spectrum that can arise in well-motived early Universe models. We showed that our method is able to accurately reconstruct $\mathcal{P}_\zeta$, especially if the peak of the SIGW is observed. However, in cases where only the infrared part of the SIGW spectrum is observed, the reconstruction suffers due to the infrared universal scaling of the spectrum of $\Omega_{\rm GW}$ for broad classes of $\mathcal{P}_\zeta$ shapes, leading to mostly prior dominated constraints. As a specific example, we applied our techniques to reconstruct the scalar spectrum leading to a GW signal fitting recent PTA data. We also tested the viability of our approach in inferring the background equation of state (assuming a perfect fluid) at the time of SIGW production, alongside the power spectrum reconstruction. The shape of the SIGW spectrum depends strongly on w, but there also exist complex degeneracies between the effects of varying w and varying $\mathcal{P}_\zeta$, which we discussed.

---

[12] The reason being that, for the case of broad peaked spectra, linear interpolation suffers from a degeneracy between the shape of $\mathcal{P}_\zeta$ and w, owing to its greater flexibility, which can result in a bias in the inferred w and $\mathcal{P}_\zeta$. The choice of GP interpolation restricts this degeneracy, by generating only smoothly varying $\mathcal{P}_\zeta$. We expect that if one were to also directly reconstruct the inflationary potential itself instead of $\mathcal{P}_\zeta$, such degeneracies would not arise since the resulting $\mathcal{P}_\zeta$ would naturally be smooth. We discuss this subject in more detail in Appendix B.

[13] Not to be confused with $x = k\eta$ in Sec. II.

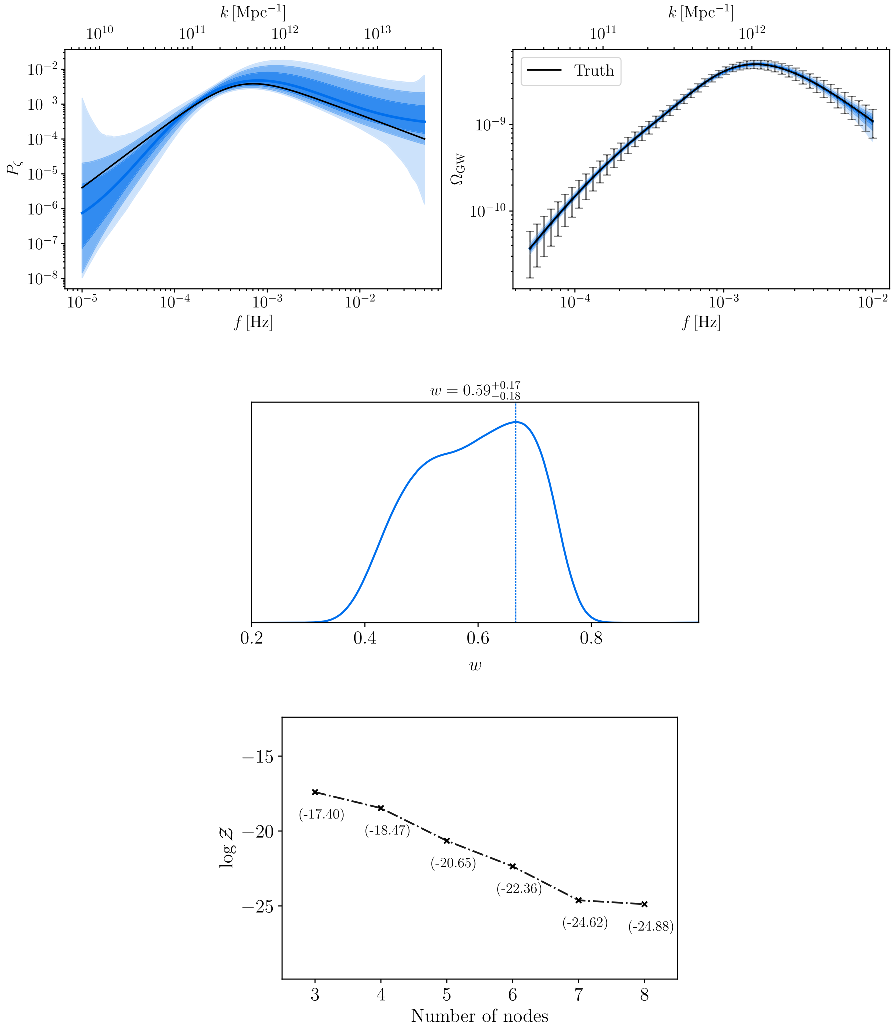

FIG. 11. Reconstruction of the BPL spectrum using GP interpolation for SIGW generated during an epoch with $w = 2/3$, see Sec. IV C. The different shaded regions correspond to 68%, 95% and 99.7% credible intervals for $\mathcal{P}_\zeta$ and $\Omega_{\rm GW}$. Reported limits represent to 95% credible intervals for the parameter w.

Our method can be extended and applied to more general situations. It would be interesting to include the effects of primordial curvature non-Gaussianities which can influence the SIGW profile (see, e.g., [70–73]). Besides curvature fluctuations, also isocurvature modes might play a role in SIGW generation (see, e.g., [74–79]). Although we focused on scalar sources, primordial tensor degrees of freedom can induce GW as well [80]. Besides considering more general primordial sources, it would also be interesting to model more accurately our priors regarding the infrared parts of the curvature and GW spectra; to include accurate constraints related to the corresponding primordial black hole formation; and to analyze how imperfect knowledge of instrumental noise might affect our results. Finally, suitable extensions of our method can allow not only to infer the $\mathcal{P}_\zeta$ profile, but also to reconstruct the inflationary scalar potential leading to SIGW profiles. We hope to return soon to these topics in separate publications.

ACKNOWLEDGMENTS

We thank Sukannya Bhattacharya, Jonas El Gammal, Gabriele Franciolini, Juan Garcia-Bellido, Jan Hamann, Marco Peloso, and David Wands for useful discussions. We are partially funded by the STFC Grants No. ST/T000813/1 and No. ST/X000648/1. A. G. is supported by the UKRI AIMLAC CDT (Artificial Intelligence, Machine Learning and Advanced Computing)-(Center for Doctoral Training), funded by Grant No. EP/S023992/1. We also acknowledge the support of the Supercomputing Wales project, which is part-funded by the European Regional Development Fund (ERDF) via Welsh Government.

DATA AVAILABILITY

The data that support the findings of this article are openly available [81].

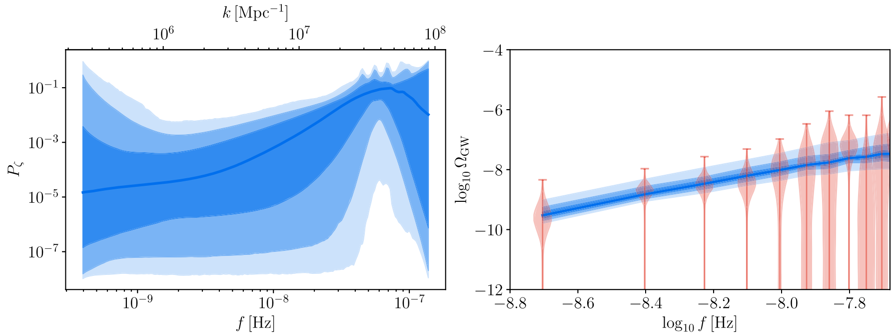

FIG. 12. Spline based reconstruction of the curvature power spectrum from PTA (NANOGrav 15 year). *Left*: The power spectrum posterior *Right*: The corresponding Ω_{GW} spectrum along with violin plots of the free spectrum Hellings Downs reconstruction from NG15.

APPENDIX A: SCALAR POWER SPECTRUM RECONSTRUCTION WITH RECENT PTA RESULTS

We test our method against real data from pulsar timing arrays.[14] We make use of the public package Ceffyl [99] to interface our code with the NANOGrav 15 year data [100,101]. The results of the reconstruction are plotted in Fig. 12. We do not find any evidence for significant deviations from a power-law $\mathcal{P}_\zeta$ or Ω_{GW} with little to choose amongst the different models, with the $\log\mathcal{Z} = -63.71, -63.66 - 63.60, -63.59, -64.57$ for $N = 2, 3, 4, 5, 6$ respectively.

APPENDIX B: GENERAL EQUATION OF STATE AND BROAD SPECTRA

In this Section we present results for the BPL example with $w = 2/3$, reconstructed using linear interpolation. We see that in addition to a peak in the posterior distribution of w at the correct value, there is an additional peak toward the $w = 1$. The reason behind this is that as w increases, the position of the peak in the SIGW spectrum shifts toward higher frequencies, and as $w, c_s \to 1$ the peak also starts to broaden. These effects are then compensated by $\mathcal{P}_\zeta$ shapes with sharp variations across the k range of the reconstruction (visible around $f \sim 10^{-4}$ Hz in the left panel of Fig. 13), which bear very little resemblance to the true curvature power spectrum. This is a consequence of the additional flexibility of the linear interpolation, as opposed to the smooth Gaussian process interpolation we employed for this example in Sec. IV. C. We expect direct reconstruction of the inflationary potential to also alleviate this issue, since in that case as well the resulting power spectrum would be much smoother compared to the linear interpolation one.

One might wonder why there is such a bias in the inferred value of w, given the dependence of the shape of the SIGW spectrum on w as seen from Eq. (4.12). In particular, for the BPL shape of the primordial curvature power spectrum, the IR part of the SIGW spectrum is independent of the IR behavior of $\mathcal{P}_\zeta$ and is determined entirely by w. However, the reason behind the bias is that for this example, the chosen error bars on Ω_{GW} imply that the IR slope of the SIGW spectrum is not precisely determined, which allows for different values of w other than the true one, to be compatible with the data.

To test this, we generate Ω_{GW} data with much lower noise values, particularly in the tails. This is given by

$$\Delta\Omega_{\mathrm{GW}}(f) = \Omega_{\mathrm{GW,obs}}(f)[0.05 + 0.01(\log f/f_*)^2]. \tag{B1}$$

This is to be contrasted with Eq. (4.1), which represented the magnitude of the error bars chosen for all other examples (except for PTA) in this work. We show in Fig. 14 the result of the w reconstruction for this low noise

---

[14] See, e.g., [82–93] for other studies. We note that the scalar induced GW interpretation of the PTA results is likely ruled out due to overproduction of PBH, at least in the case of Gaussian statistics of ζ and assuming radiation domination. The inclusion of non-Gaussianity or a nonstandard equation of state may alleviate this, as studied in Refs. [91–98].

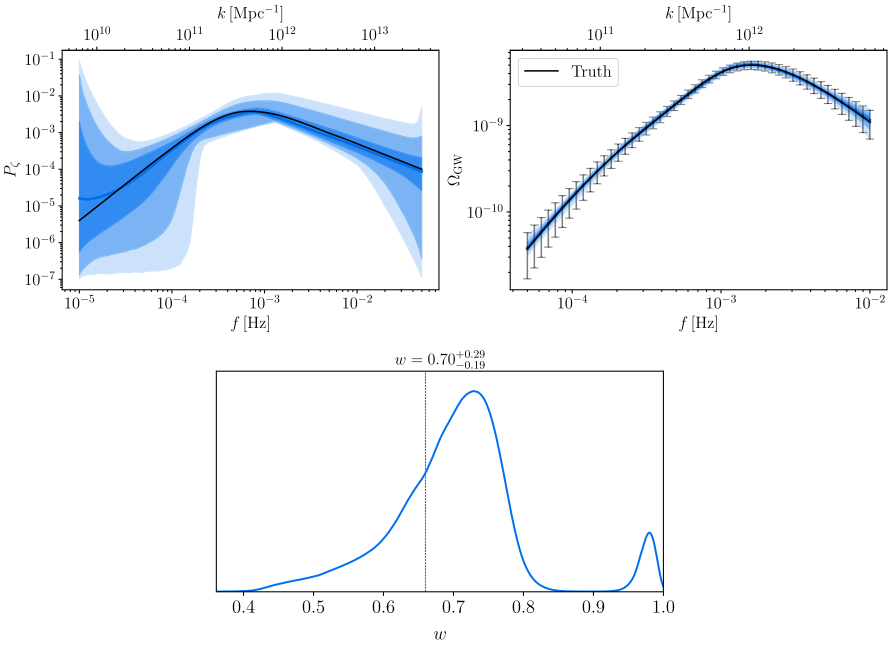

FIG. 13. Reconstruction of the BPL example using linear interpolation with five nodes, as discussed in Appendix B.

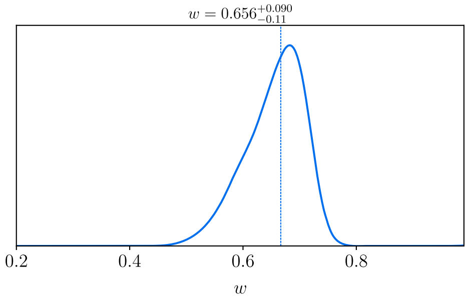

FIG. 14. Reconstruction using linear interpolation for the low noise BPL example with $w = 2/3$.

example where we see that w is now inferred correctly without any bias due to the IR slope of the SIGW spectrum being measured much more precisely.[15]

APPENDIX C: NOISY REALIZATIONS OF GW DATA

To test the robustness of our method, we also apply it to noisy realizations of the mean spectra presented in Sec. IV. A for which we generate random realizations drawn from a Gaussian distribution defined by Eq. (4.2). Our method can again recover the a curvature power spectrum close to the actual one, as long as the noise level close to the peak of the GW spectrum is low, i.e., the shape of the peak of the noisy realization is not too different from the mean spectrum. As discussed earlier, this is a consequence of the fact that the shape of the induced GW spectrum depends most strongly on the shape of the peak of the curvature power spectrum. The latter itself gets tightly constrained by the low noise levels around the peak of the GW spectrum.

The Bayesian evidence shows a clear trend for the BPL model, irrespective of the individual realization, with models with more than six nodes being favored less, as shown in Fig. 15. For brevity, we only show the reconstruction for one particular realization. We also plot the fidelity of the reconstructed P_ζ and Ω_{GW} for this realization, showing $\Delta P_\zeta \equiv |\hat{P}_\zeta - P_\zeta^{\mathrm{true}}|/P_\zeta^{\mathrm{true}}$ where $\hat{P}_\zeta$ represents the median of the reconstruction and similarly for Ω_{GW}. We see that the relative error remains small, reaching 10^{-1} or lower near the peak and only gets higher far away from it, especially in the IR for P_ζ.

For the peaked and oscillatory spectra we find that we are still able to accurately recover the underlying curvature power spectrum. However, increasing the number of nodes does not immediately lead to a decrease of the evidence independently of the random realization, owing to the increased complexity of the models, similar to what we observed with the mean-only realizations in Sec. IV. A.

---

[15] The degeneracies persist for the oscillatory model of Eq. (4.6) and are in fact much more severe, leading to bias in the inferred w even with the lower noise level example considered here.

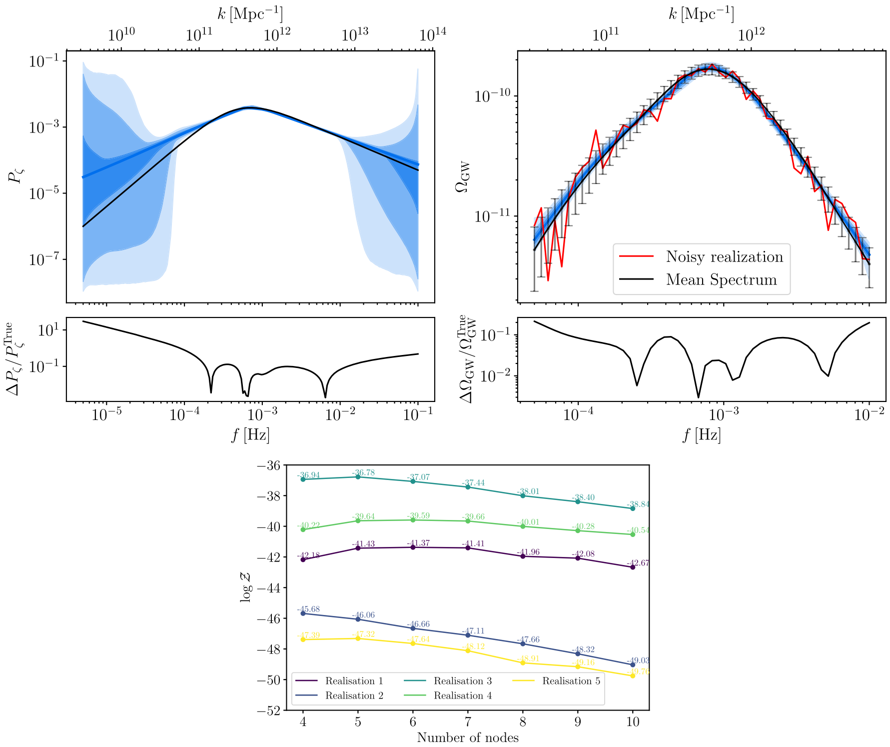

FIG. 15. *Top*: Reconstruction of the BPL spectrum for a particular noisy realization of the GW data using linear interpolation. *Bottom*: $\log \mathcal{Z}$ values across five different realizations.

[1] N. Aghanim *et al.* (Planck Collaboration), Planck 2018 results. VI. Cosmological parameters, Astron. Astrophys. **641**, A6 (2020); **652**, C4(E) (2021).

[2] S. Matarrese, O. Pantano, and D. Saez, A general relativistic approach to the nonlinear evolution of collisionless matter, Phys. Rev. D **47**, 1311 (1993).

[3] K. N. Ananda, C. Clarkson, and D. Wands, The cosmological gravitational wave background from primordial density perturbations, Phys. Rev. D **75**, 123518 (2007).

[4] D. Baumann, P. J. Steinhardt, K. Takahashi, and K. Ichiki, Gravitational wave spectrum induced by primordial scalar perturbations, Phys. Rev. D **76**, 084019 (2007).

[5] R. Saito and J. Yokoyama, Gravitational-wave constraints on the abundance of primordial black holes, Prog. Theor. Phys. **123**, 867 (2010); **126**, 351(E) (2011).

[6] E. Bugaev and P. Klimai, Induced gravitational wave background and primordial black holes, Phys. Rev. D **81**, 023517 (2010).

[7] H. Assadullahi and D. Wands, Constraints on primordial density perturbations from induced gravitational waves, Phys. Rev. D **81**, 023527 (2010).

[8] L. Alabidi, K. Kohri, M. Sasaki, and Y. Sendouda, Observable spectra of induced gravitational waves from inflation, J. Cosmol. Astropart. Phys. 09 (2012) 017.

[9] L. Alabidi, K. Kohri, M. Sasaki, and Y. Sendouda, Observable induced gravitational waves from an early matter phase, J. Cosmol. Astropart. Phys. 05 (2013) 033.

[10] J. R. Espinosa, D. Racco, and A. Riotto, A cosmological signature of the SM Higgs instability: Gravitational waves, J. Cosmol. Astropart. Phys. 09 (2018) 012.

[11] K. Kohri and T. Terada, Semianalytic calculation of gravitational wave spectrum nonlinearly induced from primordial curvature perturbations, Phys. Rev. D **97**, 123532 (2018).

[12] G. Domènech, Scalar induced gravitational waves review, Universe **7**, 398 (2021).

[13] M. Colpi *et al.* (LISA Collaboration), LISA definition study report, arXiv:2402.07571.

[14] A. Abac *et al.*, The science of the Einstein telescope, arXiv:2503.12263.

[15] O. Özsoy and G. Tasinato, Inflation and primordial black holes, Universe **9**, 203 (2023).

[16] G. Domènech, Induced gravitational waves in a general cosmological background, Int. J. Mod. Phys. D **29**, 2050028 (2020).

[17] F. Hajkarim and J. Schaffner-Bielich, Thermal history of the early universe and primordial gravitational waves from

induced scalar perturbations, Phys. Rev. D **101**, 043522 (2020).

[18] G. Domènech, S. Pi, and M. Sasaki, Induced gravitational waves as a probe of thermal history of the universe, J. Cosmol. Astropart. Phys. 08 (2020) 017.

[19] A. Ghaleb and A. Malhotra, SIGW_Inverse, GitHub repository, https://github.com/Ameek94/SIGW_Inverse/ (2025).

[20] K. Inomata, K. Kohri, T. Nakama, and T. Terada, Enhancement of gravitational waves induced by scalar perturbations due to a sudden transition from an early matter era to the radiation era, Phys. Rev. D **100**, 043532 (2019).

[21] M. Cicoli, J. P. Conlon, A. Maharana, S. Parameswaran, F. Quevedo, and I. Zavala, String cosmology: From the early universe to today, Phys. Rep. **1059**, 1 (2024).

[22] R. Allahverdi *et al.*, The first three seconds: A review of possible expansion histories of the early universe, arXiv:2006.16182.

[23] B. Batell *et al.*, Conversations and deliberations: Non-standard cosmological epochs and expansion histories, arXiv:2411.04780.

[24] J. E. Gammal *et al.* (LISA Cosmology Working Group), Reconstructing primordial curvature perturbations via scalar-induced gravitational waves with LISA, arXiv:2501.11320.

[25] K. Inomata, K. Kohri, T. Nakama, and T. Terada, Gravitational waves induced by scalar perturbations during a gradual transition from an early matter era to the radiation era, J. Cosmol. Astropart. Phys. 10 (2019) 071.

[26] M. Pearce, L. Pearce, G. White, and C. Balázs, Gravitational wave signals from early matter domination: Interpolating between fast and slow transitions, arXiv:2311.12340.

[27] M. Pearce, L. Pearce, G. White, and C. Balázs, Using gravitational wave signals to disentangle early matter dominated epochs, arXiv:2503.03101.

[28] S. Kumar, H. Tai, and L.-T. Wang, Towards a complete treatment of scalar-induced gravitational waves with early matter domination, arXiv:2410.17291.

[29] L. Alabidi, K. Kohri, M. Sasaki, and Y. Sendouda, Observable induced gravitational waves from an early matter phase, J. Cosmol. Astropart. Phys. 05 (2013) 033.

[30] H. Assadullahi and D. Wands, Gravitational waves from an early matter era, Phys. Rev. D **79**, 083511 (2009).

[31] L. T. Witkowski, SIGWFast: A Python package for the computation of scalar-induced gravitational wave spectra, arXiv:2209.05296.

[32] R. Buscicchio, E. Roebber, J. M. Goldstein, and C. J. Moore, Label switching problem in Bayesian analysis for gravitational wave astronomy, Phys. Rev. D **100**, 084041 (2019).

[33] W. J. Handley, A. N. Lasenby, H. V. Peiris, and M. P. Hobson, Bayesian inflationary reconstructions from Planck 2018 data, Phys. Rev. D **100**, 103511 (2019).

[34] Y. Akrami *et al.* (Planck Collaboration), Planck 2018 results. X. Constraints on inflation, Astron. Astrophys. **641**, A10 (2020).

[35] R. Trotta, Bayes in the sky: Bayesian inference and model selection in cosmology, Contemp. Phys. **49**, 71 (2008).

[36] J. Skilling, Nested Sampling, in *Bayesian Inference and Maximum Entropy Methods in Science and Engineering: 24th International Workshop on Bayesian Inference and Maximum Entropy Methods in Science and Engineering*, edited by R. Fischer, R. Preuss, and U. V. Toussaint, vol. 735 of American Institute of Physics Conference Series (AIP, 2004), pp. 395–405.

[37] M. P. Hobson, A. H. Jaffe, A. R. Liddle, P. Mukherjee, and D. Parkinson, *Bayesian Methods in Cosmology* (Cambridge University Press, Cambridge, England, 2009).

[38] G. Ashton *et al.*, Nested sampling for physical scientists, Nature (London) **2**, 39 (2022).

[39] W. J. Handley, M. P. Hobson, and A. N. Lasenby, PolyChord: Next-generation nested sampling, Mon. Not. R. Astron. Soc. **453**, 4385 (2015).

[40] W. J. Handley, M. P. Hobson, and A. N. Lasenby, PolyChord: Nested sampling for cosmology, Mon. Not. R. Astron. Soc. **450**, L61 (2015).

[41] J. U. Lange, Nautilus: Boosting Bayesian importance nested sampling with deep learning, Mon. Not. R. Astron. Soc. **525**, 3181 (2023).

[42] C. Caprini, D. G. Figueroa, R. Flauger, G. Nardini, M. Peloso, M. Pieroni, A. Ricciardone, and G. Tasinato, Reconstructing the spectral shape of a stochastic gravitational wave background with LISA, J. Cosmol. Astropart. Phys. 11 (2019) 017.

[43] R. Flauger, N. Karnesis, G. Nardini, M. Pieroni, A. Ricciardone, and J. Torrado, Improved reconstruction of a stochastic gravitational wave background with LISA, J. Cosmol. Astropart. Phys. 01 (2021) 059.

[44] O. Hartwig, M. Lilley, M. Muratore, and M. Pieroni, Stochastic gravitational wave background reconstruction for a nonequilateral and unequal-noise LISA constellation, Phys. Rev. D **107**, 123531 (2023).

[45] T. Knapp, P. M. Meyers, and A. I. Renzini, A model-agnostic gravitational-wave background characterization algorithm, arXiv:2507.08095.

[46] A. Santini, M. Muratore, J. Gair, and O. Hartwig, A flexible, GPU-accelerated approach for the joint characterization of LISA instrumental noise and stochastic gravitational wave backgrounds, arXiv:2507.06300.

[47] C. Caprini, R. Jinno, M. Lewicki, E. Madge, M. Merchand, G. Nardini, M. Pieroni, A. Roper Pol, and V. Vaskonen (LISA Cosmology Working Group), Gravitational waves from first-order phase transitions in LISA: Reconstruction pipeline and physics interpretation, J. Cosmol. Astropart. Phys. 10 (2024) 020.

[48] M. Braglia *et al.* (LISA Cosmology Working Group), Gravitational waves from inflation in LISA: Reconstruction pipeline and physics interpretation, J. Cosmol. Astropart. Phys. 11 (2024) 032.

[49] A. Marriott-Best, D. Chowdhury, A. Ghoshal, and G. Tasinato, Exploring cosmological gravitational wave backgrounds through the synergy of LISA and the Einstein telescope, Phys. Rev. D **111**, 103001 (2025).

[50] C. Caprini, R. Durrer, T. Konstandin, and G. Servant, General properties of the gravitational wave spectrum from phase transitions, Phys. Rev. D **79**, 083519 (2009).

[51] R.-G. Cai, S. Pi, and M. Sasaki, Universal infrared scaling of gravitational wave background spectra, Phys. Rev. D **102**, 083528 (2020).

[52] C. Yuan, Z.-C. Chen, and Q.-G. Huang, Log-dependent slope of scalar induced gravitational waves in the infrared regions, Phys. Rev. D **101**, 043019 (2020).

[53] G. Domènech and J. Chluba, Regularizing the induced GW spectrum with dissipative effects, arXiv:2503.13670.

[54] C. T. Byrnes, P. S. Cole, and S. P. Patil, Steepest growth of the power spectrum and primordial black holes, J. Cosmol. Astropart. Phys. 06 (2019) 028.

[55] O. Özsoy and G. Tasinato, On the slope of the curvature power spectrum in non-attractor inflation, J. Cosmol. Astropart. Phys. 04 (2020) 048.

[56] P. Carrilho, K. A. Malik, and D. J. Mulryne, Dissecting the growth of the power spectrum for primordial black holes, Phys. Rev. D **100**, 103529 (2019).

[57] G. Tasinato, An analytic approach to non-slow-roll inflation, Phys. Rev. D **103**, 023535 (2021).

[58] G. Tasinato, Large $|\eta|$ approach to single field inflation, Phys. Rev. D **108**, 043526 (2023).

[59] M. Cielo, G. Mangano, O. Pisanti, and D. Wands, Steepest growth in the primordial power spectrum from excited states at a sudden transition, J. Cosmol. Astropart. Phys. 04 (2025) 007.

[60] J. Fumagalli, S. e. Renaux-Petel, and L. T. Witkowski, Resonant features in the stochastic gravitational wave background, J. Cosmol. Astropart. Phys. 08 (2021) 059.

[61] L. T. Witkowski, G. Domènech, J. Fumagalli, and S. Renaux-Petel, Expansion history-dependent oscillations in the scalar-induced gravitational wave background, J. Cosmol. Astropart. Phys. 05 (2022) 028.

[62] M. Braglia, X. Chen, and D. K. Hazra, Probing primordial features with the stochastic gravitational wave background, J. Cosmol. Astropart. Phys. 03 (2021) 005.

[63] E. Bagui *et al.* (LISA Cosmology Working Group), Primordial black holes and their gravitational-wave signatures, Living Rev. Relativity **28**, 1 (2025).

[64] H. Assadullahi and D. Wands, Gravitational waves from an early matter era, Phys. Rev. D **79**, 083511 (2009).

[65] M. Pearce, L. Pearce, G. White, and C. Balázs, Gravitational wave signals from early matter domination: Interpolating between fast and slow transitions, arXiv:2311.12340.

[66] M. Pearce, L. Pearce, G. White, and C. Balázs, Using gravitational wave signals to disentangle early matter dominated epochs, arXiv:2503.03101.

[67] C. T. Byrnes, M. Hindmarsh, S. Young, and M. R. S. Hawkins, Primordial black holes with an accurate QCD equation of state, J. Cosmol. Astropart. Phys. 08 (2018) 041.

[68] G. Franciolini, D. Racco, and F. Rompineve, Footprints of the QCD crossover on cosmological gravitational waves at pulsar timing arrays, Phys. Rev. Lett. **132**, 081001 (2024); **133**, 189901(E) (2024).

[69] C. K. Williams and C. E. Rasmussen, *Gaussian Processes for Machine Learning* (MIT Press, Cambridge, MA, 2006).

[70] C. Unal, Imprints of primordial non-Gaussianity on gravitational wave spectrum, Phys. Rev. D **99**, 041301 (2019).

[71] R.-g. Cai, S. Pi, and M. Sasaki, Gravitational waves induced by non-Gaussian scalar perturbations, Phys. Rev. Lett. **122**, 201101 (2019).

[72] P. Adshead, K. D. Lozanov, and Z. J. Weiner, Non-Gaussianity and the induced gravitational wave background, J. Cosmol. Astropart. Phys. 10 (2021) 080.

[73] G. Perna, C. Testini, A. Ricciardone, and S. Matarrese, Fully non-Gaussian scalar-induced gravitational waves, J. Cosmol. Astropart. Phys. 05 (2024) 086.

[74] G. Domènech, Cosmological gravitational waves from isocurvature fluctuations, AAPPS Bull. **34**, 4 (2024).

[75] S. Passaglia and M. Sasaki, Primordial black holes from CDM isocurvature perturbations, Phys. Rev. D **105**, 103530 (2022).

[76] G. Domènech, S. Passaglia, and S. Renaux-Petel, Gravitational waves from dark matter isocurvature, J. Cosmol. Astropart. Phys. 03 (2022) 023.

[77] A. Marriott-Best, M. Peloso, and G. Tasinato, New gravitational wave probe of vector dark matter, arXiv:2502.13116.

[78] O. Özsoy and G. Tasinato, Vector dark matter, inflation, and non-minimal couplings with gravity, J. Cosmol. Astropart. Phys. 06 (2024) 003.

[79] Z.-C. Chen and L. Liu, Can we distinguish between adiabatic and isocurvature fluctuations with pulsar timing arrays?, Sci. China Phys. Mech. Astron. **68**, 250412 (2025).

[80] P. Bari, N. Bartolo, G. Domènech, and S. Matarrese, Gravitational waves induced by scalar-tensor mixing, Phys. Rev. D **109**, 023509 (2024).

[81] A. Ghaleb and A. Malhotra, SIGW_Inverse, 2025, https://github.com/Ameek94/SIGW_Inverse/.

[82] A. Afzal *et al.* (NANOGrav Collaboration), The NANOGrav 15 yr data set: Search for signals from new physics, Astrophys. J. Lett. **951**, L11 (2023); **971**, L27(E) (2024).

[83] J. Antoniadis *et al.* (EPTA and InPTA Collaborations), The second data release from the European pulsar timing array—IV. Implications for massive black holes, dark matter, and the early Universe, Astron. Astrophys. **685**, A94 (2024).

[84] D. G. Figueroa, M. Pieroni, A. Ricciardone, and P. Simakachorn, Cosmological background interpretation of pulsar timing array data, Phys. Rev. Lett. **132**, 171002 (2024).

[85] J. Ellis, M. Fairbairn, G. Franciolini, G. Hütsi, A. Iovino, M. Lewicki, M. Raidal, J. Urrutia, V. Vaskonen, and H. Veermäe, What is the source of the PTA GW signal?, Phys. Rev. D **109**, 023522 (2024).

[86] Y.-F. Cai, X.-C. He, X.-H. Ma, S.-F. Yan, and G.-W. Yuan, Limits on scalar-induced gravitational waves from the stochastic background by pulsar timing array observations, Sci. Bull. **68**, 2929 (2023).

[87] Z. Yi, Q. Gao, Y. Gong, Y. Wang, and F. Zhang, Scalar induced gravitational waves in light of pulsar timing array data, Sci. China Phys. Mech. Astron. **66**, 120404 (2023).

[88] Z. Yi, Z.-Q. You, and Y. Wu, Model-independent reconstruction of the primordial curvature power spectrum from PTA data, J. Cosmol. Astropart. Phys. 01 (2024) 066.

[89] H. Firouzjahi and A. Talebian, Induced gravitational waves from ultra slow-roll inflation and pulsar timing

arrays observations, J. Cosmol. Astropart. Phys. 10 (2023) 032.

[90] L. Liu, Z.-C. Chen, and Q.-G. Huang, Probing the equation of state of the early Universe with pulsar timing arrays, J. Cosmol. Astropart. Phys. 11 (2023) 071.

[91] S. Wang, Z.-C. Zhao, J.-P. Li, and Q.-H. Zhu, Implications of pulsar timing array data for scalar-induced gravitational waves and primordial black holes: Primordial non-Gaussianity fNL considered, Phys. Rev. Res. **6**, L012060 (2024).

[92] G. Domènech, S. Pi, A. Wang, and J. Wang, Induced gravitational wave interpretation of PTA data: A complete study for general equation of state, J. Cosmol. Astropart. Phys. 08 (2024) 054.

[93] K. Harigaya, K. Inomata, and T. Terada, Induced gravitational waves with kination era for recent pulsar timing array signals, Phys. Rev. D **108**, 123538 (2023).

[94] S. Balaji, G. Domènech, and G. Franciolini, Scalar-induced gravitational wave interpretation of PTA data: The role of scalar fluctuation propagation speed, J. Cosmol. Astropart. Phys. 10 (2023) 041.

[95] G. Franciolini, A. Iovino, Jr.,, V. Vaskonen, and H. Veermae, Recent gravitational wave observation by pulsar timing arrays and primordial black holes: The importance of non-Gaussianities, Phys. Rev. Lett. **131**, 201401 (2023).

[96] L. Liu, Z.-C. Chen, and Q.-G. Huang, Implications for the non-Gaussianity of curvature perturbation from pulsar timing arrays, Phys. Rev. D **109**, L061301 (2024).

[97] L. Liu, Y. Wu, and Z.-C. Chen, Simultaneously probing the sound speed and equation of state of the early Universe with pulsar timing arrays, J. Cosmol. Astropart. Phys. 04 (2024) 011.

[98] R. Inui, C. Joana, H. Motohashi, S. Pi, Y. Tada, and S. Yokoyama, Primordial black holes and induced gravitational waves from logarithmic non-Gaussianity, J. Cosmol. Astropart. Phys. 03 (2025) 021.

[99] W. G. Lamb, S. R. Taylor, and R. van Haasteren, Rapid refitting techniques for Bayesian spectral characterization of the gravitational wave background using pulsar timing arrays, Phys. Rev. D **108**, 103019 (2023).

[100] The NANOGrav Collaboration, The NANOGrav 15 year data set, https://zenodo.org/records/16051178.

[101] G. Agazie *et al.* (NANOGrav Collaboration), The NANOGrav 15 yr data set: Evidence for a gravitational-wave background, Astrophys. J. Lett. **951**, L8 (2023).